Department of Applied Physics

# Defect studies in n-type indium nitride

---

**Christian Rauch**

Aalto University

DOCTORAL DISSERTATIONS

Aalto University publication series
**DOCTORAL DISSERTATIONS** 52/2012

# Defect studies in n-type indium nitride

**Christian Rauch**

Doctoral dissertation for the degree of Doctor of Science in Technology to be presented with due permission of the School of Science for public examination and debate in Auditorium F at the Aalto University School of Science (Espoo, Finland) on the 4th of May 2012 at 13 o'clock.

**Aalto University**
**School of Science**
**Department of Applied Physics**
**Defect Spectroscopy and Positron Physics Group**

**Supervisors**
Prof. Martti Puska
Department of Applied Physics
School of Science
Aalto University

**Instructors**
Prof. Filip Tuomisto
Department of Applied Physics
School of Science
Aalto University

**Preliminary examiners**
Prof. Kai Nordlund
Department of Physics
University of Helsinki
Helsinki, Finland

Dr. Marie-France Barthe
Conditions Extrêmes et Matériaux: Haute Température et Irradiation
Centre national de la recherche scientifique
Orléans, France

**Opponents**
Prof. Czeslaw Skierbiszewski
Institute of High Pressure Physics
Polish Academy of Sciences
Warsaw, Poland

Aalto University publication series
**DOCTORAL DISSERTATIONS** 52/2012

ISBN 978-952-60-4606-8 (printed)
ISBN 978-952-60-4607-5 (pdf)
ISSN-L 1799-4934
ISSN 1799-4934 (printed)
ISSN 1799-4942 (pdf)

Unigrafia Oy
Helsinki 2012

Finland

The dissertation can be read at http://lib.tkk.fi/Diss/

NORDIC ECOLABEL
441 697
Printed matter

**Aalto University**

**Aalto University, P.O. Box 11000, FI-00076 Aalto** www.aalto.fi

# Abstract

**Author**
Christian Rauch

**Name of the doctoral dissertation**
Defect studies in n-type indium nitride

**Publisher** School of Science

**Unit** Department of Applied Physics

**Series** Aalto University publication series DOCTORAL DISSERTATIONS 52/2012

**Field of research** Engineering Physics, Physics

**Manuscript submitted** 28 February 2012 **Manuscript revised** 18 April 2012

**Date of the defence** 4 May 2012 **Language** English

☐ **Monograph** ☒ **Article dissertation (summary + original articles)**

## Abstract

Sparked by the discovery of its narrow bandgap, indium nitride (InN) has recently attracted major scientific interest as a promising material in opto- and high-speed electronics. Industrial application, however, is hampered by the material's strong propensity for n-type conductivity and high defect concentrations. Despite major research efforts in that area, relatively little is known about the properties of defects in InN.The main goal of this thesis was to study the formation and characteristics of native point defects in n-type InN and investigate their role for the material's electrical properties. Positron annihilation spectroscopy was used as the main experimental technique for defect characterization. By combining density functional theory calculations with experimental positron annihilation methods, the dominant vacancy-type positron traps in common InN material were identified. As-grown and n-doped InN layers that were deposited by different growth methods, as well as irradiated and annealed material with varying carrier concentrations, were analyzed to investigate the formation and evolution of point defects in different environments. The data were compared to results from complementary techniques in order to study the interplay of point and extended defects, and their role in limiting the conductivity in n-type InN.

It is found that isolated indium (In) vacancies and their complexes are the dominant vacancy-type positron traps in InN. Isolated In vacancies are introduced in high-energy particle irradiation of InN, and anneal out at moderate temperatures if not stabilized by one or more nitrogen (N) vacancies. In-N vacancy complexes are the dominant vacancy-type positron traps in as-grown InN. In state-of-the-art material with low free electron concentrations, their concentration is at or below the detection limit of positron annihilation methods. For increasing free electron concentration, an enhanced formation of these vacancy complexes is observed, which act as significant source of compensation and scattering centers in highly n-type material. Additionally, a high density of negatively charged defects with only small effective open-volume is found that is tentatively attributed to negatively charged N vacancies. Estimated defect densities are significantly higher than what is expected from thermodynamic considerations, which suggests that alternative defect formation mechanisms determine the point defect densities in the material.

**Keywords** Indium nitride, n-type, defects, vacancies, positron annihilation, density functional theory

**ISBN (printed)** 978-952-60-4606-8 **ISBN (pdf)** 978-952-60-4607-5

**ISSN-L** 1799-4934 **ISSN (printed)** 1799-4934 **ISSN (pdf)** 1799-4942

**Location of publisher** Espoo **Location of printing** Helsinki **Year** 2012

**Pages** 131 **The dissertation can be read at** http://lib.tkk.fi/Diss/

# Preface

The work presented in this thesis was mainly carried out in the Positron Physics and Defect Spectroscopy group at the Department of Applied Physics at Aalto University, Helsinki (Finland). It has been conducted in close collaboration with European partner laboratories inside the Marie Curie Initial Training Network "High quality material and intrinsic properties of InN and indium rich nitride alloys" (RAINBOW) during the years 2008–2012. Funding of the European Commission under the 7th Framework Program, Contract No. PITN-Ga-2008-213238, is acknowledged.

I would like to express my gratitude to Prof. Martti Puska for the supervision of this work, and to my instructor Prof. Filip Tuomisto for his continuous support and the opportunity to work in his group. A big thanks to Dr. Ilja Makkonen for introducing me to computational methods of materials physics, and to Dr. Floris Reurings and Dr. Klaus Rytsölä for their help with the experimental equipment, amongst others. Thanks also to all my past and present colleagues and collaborators inside and outside Aalto University and the RAINBOW network for an inspiring working atmosphere, and to all others who are not mentioned by name but contributed to the realization of this work.

I am grateful to my family and friends for their support and encouragement. Above all, thanks to Heini-Tuuli.

Helsinki, April 19, 2012,

Christian Rauch

# Contents

# List of Publications

This thesis consists of an overview and of the following publications which are referred to in the text by their Roman numerals.

**I** C. Rauch, F. Reurings, F. Tuomisto, T. D. Veal, C. F. McConville, H. Lu, W. J. Schaff, C. S. Gallinat, G. Koblmüller, J. S. Speck, W. Egger, B. Löwe, L. Ravelli, and S. Sojak. In-vacancies in Si-doped InN. *Physica Status Solidi A*, 207, 1083, pages 1–4, November 2010.

**II** F. Reurings, C. Rauch, F. Tuomisto, R. E. Jones, K. M. Yu, W. Walukiewicz, and W. J. Schaff. Defect redistribution in postirradiation rapid-thermal-annealed InN. *Physical Review B*, 82, 153202, pages 1–4, October 2010.

**III** C. Rauch, I. Makkonen, and F. Tuomisto. Identifying vacancy complexes in compound semiconductors with positron annihilation spectroscopy: a case study of InN. *Physical Review B*, 84, 125201 pages 1–9, September 2011.

**IV** C. Rauch, Ö. Tuna, C. Giessen, M. Heuken, and F. Tuomisto. Point defect evolution in low-temperature MOCVD growth of InN. *Physica Status Solidi A*, 209, 87, pages 1–4, November 2011.

**V** C. Rauch, F. Tuomisto, A. Vilalta-Clemente, B. Lacroix, P. Ruterana, S. Kraeusel, B. Hourahine, and W. J. Schaff. Defect evolution and interplay in n-type InN. *Applied Physics Letters*, 100, 091907, pages 1–3, March 2012.

**VI** C. Rauch, F. Tuomisto, P. D. C. King, T. Veal, H. Lu, and W. J. Schaff. Self-compensation in highly n-type InN. *arXiv:1204.3299v1 [cond-mat.mtrl-sci]*, pages 1–5, April 2012.

# Author's Contribution

## Publication I: "In-vacancies in Si-doped InN"

The author has been involved in the planning of all experiments and performed the Doppler broadening measurements. He has analyzed the experimental data, contributed significantly to the interpretation of the results, and wrote the first draft of the manuscript.

## Publication II: "Defect redistribution in postirradiation rapid-thermal-annealed InN"

The author performed the analysis and fitting of the temperature dependent Doppler broadening measurements. He has contributed significantly to the interpretation of the published results and wrote part of the manuscript.

## Publication III: "Identifying vacancy complexes in compound semiconductors with positron annihilation spectroscopy: a case study of InN"

The author has planned and performed all experiments and performed all computational work. He has contributed significantly to the interpretation of the results and wrote the first draft of the manuscript.

## Publication IV: "Point defect evolution in low-temperature MOCVD growth of InN"

The author has been involved in planning of all phases of the study, and performed and analyzed the Doppler broadening measurements. He has contributed significantly to the interpretation of the results and wrote the first draft of the manuscript.

## Publication V: "Defect evolution and interplay in n-type InN"

The author has been involved in planning of all phases of the study, performed and analyzed the Doppler broadening measurements, and participated in the computational work. He has contributed significantly to the interpretation of the results and wrote the first draft of the manuscript.

## Publication VI: "Self-compensation in highly n-type InN"

The author has been involved in planning of all phases of the study, performed and analyzed the Doppler broadening measurements, and participated in the analysis of the mobility data. He has contributed significantly to the interpretation of the results and wrote the first draft of the manuscript.

# List of Figures

# 1. Introduction

*"Crystals are like people, it is their defects
that make them interesting."* F. C. Franck.

Crystalline semiconductors are the backbone of modern electronics and form the heart of such seemingly different devices as computer chips, mobile phones, modern TV screens and displays, light emitting diodes (LED's) and solar cells. In fact, modern technology is hard to imagine without them. The fundamental property of semiconductors is their ability to either block or conduct the flow of electricity. By skillful combination of conducting and non-conducting semiconductor layers with thicknesses as small as a few atoms, basic logic devices and switches are formed which can be combined into larger units called integrated circuits (IC's). What started out with a modest number of only a few relatively large transistors in the early 1970's, has today reached an impressive degree of miniaturization and integration with more than 3 000 000 transistors per mm$^2$ in modern microchips [1]. The relevance of solid control of the material quality in such high-performance devices comes without saying.

Imperfections in the ideal structure of a crystal are called defects. These include intrinsic modifications as well as external impurities incorporated into the host crystal's lattice. Microscopic defects are present in all crystalline materials. Even in only small concentrations of a few parts per million (ppm), their presence significantly influences or even determines macroscopic quantities such as the strength or hardness of a material. Effects are not limited to mechanical properties. Modifications in the crystal structure can directly affect a material's electronic, magnetic and optical characteristics such as its conductivity, color or type of magnetism. Therefore, it is evident that no material technology is possible without sufficient control and knowledge of the material's defect properties. Manipulation of crystal defects, e.g., through the deliberate introduction of impurity atoms (doping), forms the basis of the most fundamental devices in semiconductor technology and, hence, the key for its application in modern (opto-) electronics.

While early semiconductor technology was nearly entirely built on silicon (Si) as the source material, diversification in the last few decades led to the emergence of a variety of new materials with favorable properties in specific areas. The III-nitride compound semiconductors indium nitride (InN), gallium nitride (GaN) and aluminum nitride (AlN) are an ideal material system for optoelectronic devices [2, 3]. By alloying InN with GaN or AlN, the systems' light emitting and absorbing capacities can be tailored to span the whole visible range of the electromagnetic spectrum and, hence, serve as an ideal basis for the fabrication of high-efficiency solar cells or white LED's.

InN has long been the least studied III-nitride. Early material was grown mainly by radio-frequency (RF) sputtering that produced dominantly polycrystalline samples with high electron concentrations and an absorption edge at $\sim$1.2 $\mu$m [4, 5]. This led to the assumption of a value of 1.89 eV for the bandgap of InN [6]. In the early 2000's, improvements in InN growth made single crystalline InN layers available with significantly enhanced crystal quality and much lower absorption edges. Based on optical absorption, photoluminescence (PL), and photoluminescence excitation (PLE) measurements of single crystalline InN layers grown by plasma-assisted molecular beam epitaxy (PAMBE), Davydov *et al.* [7] proposed in 2002 a reduced bandgap of InN of $\sim$0.9 eV, which was soon corrected down to the now accepted value of 0.64 eV at room-temperature [4, 8]. The discovery of the narrow bandgap of InN sparked significant scientific and industrial interest in the field of InN and In-rich III-nitrides. In recent years, many important discoveries on the basic characteristics of the material were made and promising physical properties were revealed. Among the key challenges in InN research is its high defect density combined with a strong propensity for n-type conductivity. The microscopic origins are still unknown and large efforts have been made in the investigation of the defect landscape of the material.

Positron annihilation spectroscopy is a powerful tool for the investigation of point defects in semiconductors [9–12]. Positrons can get trapped and annihilate at neutral and negatively charged open volume sites as well as negatively charged ions in the crystal lattice due to a locally reduced Coulomb repulsion. This increases the positron lifetime and narrows the momentum distribution of annihilating electron-positron (e-p) pairs, both of which can be measured by recording the emitted annihilation $\gamma$ radiation. Through analysis of the line-shape of the annihilation radiation or the positron lifetime spectrum, important information on the physical properties at the annihilation site can be deduced and the density, identity or charge of the positron trapping defect may be identified.

In this work, positron annihilation spectroscopy has been used to study the properties of vacancy-type point defects in n-type InN. A new methodology for defect identification in novel semiconductor materials has been developed, using a combination of experimental positron annihilation methods with comprehensive density functional theory (DFT) calculations of positron trapping and annihilation. In Publications I and II, Doppler broadening and positron lifetime spectroscopy were performed to investigate the defects in Si-doped and irradiated MBE-grown InN layers, respectively, with increasing free electron concentrations up to $6.6\times10^{20}$ $\text{cm}^{-3}$. In Pub. III, the annihilation properties of dominant vacancy-type positron traps in InN have been calculated with DFT and the results were compared to experimental spectra in order to identify the dominant positron traps in common InN samples. In Pub. IV, point defects in low-temperature MOCVD grown InN layers are investigated. The defect evolution and interplay of point and extended defects in the n-type Si-doped and irradiated samples were analyzed in Pub. V. Temperature dependent Doppler broadening measurements are used in Pub. VI to determine the concentration of dominant acceptor type defects in these samples, and combined with Hall effect measurements to investigate compensation mechanisms in n-type InN.

In the following, a summary of the main concepts and results of this work is presented. In Ch. 2, the material InN is introduced. Chapter 3 summarizes important aspects of the physics of defects in semiconductors. The main experimental technique for this work, positron annihilation spectroscopy, is described in Ch. 4. Tools for the computational treatment of positron annihilation in semiconductors are outlined in Ch. 5. In Ch. 6, computational and experimental positron annihilation methods are combined to identify the dominant vacancy-type positron traps in InN. In Ch. 7, these results are applied to the study of the evolution and interplay of point and extended defects in n-type Si-doped and irradiated MBE-grown layers, as well as in MOCVD grown material. Chapter 8 summarizes the results on the role of vacancy defects as compensating centers in n-type InN.

# 2. Indium nitride: properties and challenges, samples

Indium nitride (InN) is a significantly cation-anion mismatched III-V compound semiconductor with a direct bandgap of 0.64 eV [14] at room-temperature. In alloys with wide bandgap aluminum nitride (AlN), $E_{\mathrm{G}}$ = 6.2 eV, and gallium nitride (GaN), $E_{\mathrm{G}}$ = 3.4 eV, it extends the optical range of III-nitrides from the ultraviolet (UV) at 0.2 $\mu$m to the near infrared (IR) at $\sim$1.9 $\mu$m [4], covering the whole visible spectrum (Fig. 2.1). Combined with a high optical efficiency [15], this makes III-nitrides a key material system in optoelectronic industry for the development of applications such as (white) light emitting diodes and high-efficiency multi-junction solar cells [2–4, 16–18]. Recently, InN has also attracted significant interest on its own right because of its low electron effective mass [4, 5] and surface electron accumulation layer [19, 20], amongst others. InN possesses good electron transport properties and is an interesting material for the fabrication of high-frequency devices like high-electron-mobility transistors [3, 21–23].

In the following chapter, an introduction to InN growth (Sect. 2.1), its lattice and band structure (Sect. 2.2), optical and electrical properties (Sect. 2.3), as well as defects and doping related issues (Sect. 2.3) is given. For a more comprehensive review please see Refs. [4, 5]. A short overview of the investigated InN samples is presented in Sect. 2.5.

## 2.1 Growth and substrates

The growth of InN is very challenging. With a binding energy of only 1.93 eV for the In-N bond, InN is the least stable material in the III-nitride family [5]. This low In-N binding energy results in a low dissociation temperature of the material and therefore in severe limitations

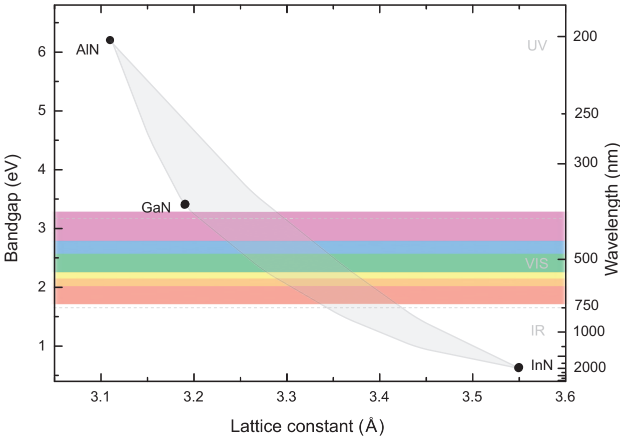

**Figure 2.1.** Bandgap energies as a function of the lattice constants in AlN, GaN, InN and their alloys. The visible range of the electromagnetic spectrum extends from ∼390 to 750 nm, i.e., well within the bandgaps of $Ga_xIn_{1-x}N$ and $Al_xIn_{1-x}N$ [4, 13].

in the maximum growth temperature. At the low temperature end, the growth temperature is limited by the high equilibrium vapor pressure of InN and a sufficient surface ad-atom mobility during growth. Finding a good compromise between these contradicting requirements is a key challenge common for all InN growth methods.

The most popular techniques used for the preparation of InN crystals are molecular beam epitaxy (MBE) [24–26] and metal organic chemical vapor deposition (MOCVD) [27–30]. Most MOCVD and MBE samples are grown in the temperature range of 500–600°C [30] and 450–550°C [26], respectively, which is very low compared to common growth temperatures of, e.g., Si or GaN [31]. In MBE growth, big improvements in the layer quality could be achieved through switching the nitrogen source from $NH_3$ to atomic N supplied by nitrogen plasma sources in plasma assisted molecular beam epitaxy (PAMBE) [26]. As of today, the highest quality InN layers available have been grown with this technique [4]. MOCVD growth has important advantages for industrial applications due to its good scalability, but still suffers from inferior material quality and a low growth rate [29].

The most commonly used substrate in InN epitaxy is sapphire, which is available in large area wafers at relatively low cost and high quality. However, challenges arise from the large lattice mismatch (∼25%) and difference in thermal expansion coefficients between sapphire and

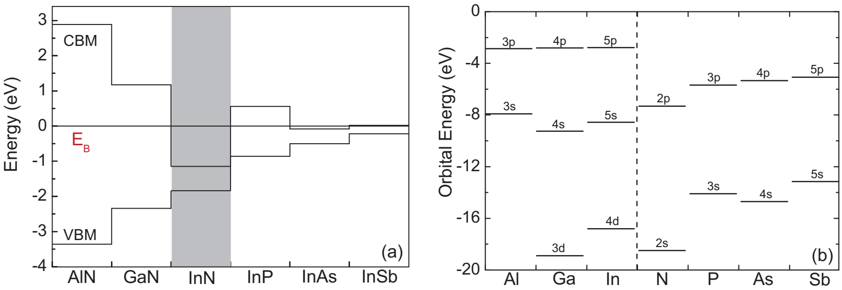

**Figure 2.2.** (a) Energy of conduction and valence band edges of III-N and In-V compounds with respect to the branch point energy. (b) Energy of constituent atomic orbitals [36, 37].

InN [5]. This can result in high densities of strain-relieving structural defects [32, 33]. The use of appropriate (low-temperature) buffer layers (e.g., AlN, GaN, InN) has been shown to significantly improve the quality of the deposited InN layer [24, 34]. Alternative popular substrate materials for InN growth include GaN templates and Si(111). Very high crystal quality layers could be achieved using GaN [5], but these templates are very costly. Si has strong advantages as a substrate because of its high purity, availability and the already established production schemes, but InN layers grown on Si have long suffered from relatively poor quality compared to those grown on sapphire [35].

## 2.2 Lattice and band structure

InN crystallizes in the hexagonal wurtzite lattice [4, 5] that consists of two hexagonal close packed (HCP) sub-lattices of In and N atoms in $C_{6\mathrm{V}}^4$ symmetry. The basic lattice constants are $a = 3.5365$ Å and $c = 5.70399$ Å [7]. In this structure each atom is four-fold coordinated. The strong uniaxial nature in combination with the partially ionic bonding leads to a strong piezoelectric polarization along the c-axis [38]. Through appropriate choice of substrate and growth conditions, crystallization in the cubic zincblende structure ($T_d^2$) has also been achieved [39–42].

Wurtzite InN has a direct bandgap of 0.64 eV. The narrow bandgap results in strong non-parabolicity (Fig. 2.3) of the conduction band (CB) which is caused by $\mathbf{k} \cdot \mathbf{p}$ repulsion between the $p$-like valence band and the $s$-like conduction band [43]. Applying Kane's two band $\mathbf{k} \cdot \mathbf{p}$ model [44] and neglecting spin-orbit coupling ($\Delta_{\mathrm{so}}$) and crystal-field splitting ($\Delta_{\mathrm{cr}}$), Wu *et al.* [45] calculated the CB dispersion relation with respect to the valence band maximum (VBM) as

$$E_{\mathrm{C}}(k) = E_{\mathrm{G}} + \frac{\hbar^2 k^2}{2m_0} + \frac{1}{2}\left(\sqrt{E_{\mathrm{G}}^2 + 4E_{\mathrm{P}}\frac{\hbar^2 k^2}{2m_0}} - E_{\mathrm{G}}\right), \tag{2.1}$$

where $E_{\mathrm{G}}$ = 0.64eV is the intrinsic bandgap of InN, and $E_{\mathrm{P}}$ the $\mathbf{k} \cdot \mathbf{p}$ interaction energy. The density of states effective mass is then a function of *k*,

$$m^*(k) = \frac{\hbar^2 k^2}{dE_{\mathrm{C}}(k)/\mathrm{d}k}. \tag{2.2}$$

At the bottom of the CB a small electron effective mass of $\frac{m_{\mathrm{e}}^*}{m_0} = 0.07 \pm 0.02$ has been determined by plasma reflection spectroscopy [45]. Non-parabolicity of the conduction band starts to play an important role for $k > 0.05$ Å$^{-1}$, or $n > 10^{19}$ cm$^{-3}$. A direct consequence of the strongly non-parabolic conduction band of InN is its increased density of states compared to the parabolic case. This results in a less pronounced change of the Fermi energy with increasing electron concentration, which can also be observed in the shift of the absorption edge in n-type samples.

The small value of the InN bandgap caused initial confusion as it breaks the empirical common-cation rule with respect to the bandgap of indium phosphide [$E_{\mathrm{G}}$ (InP) = 1.46 eV [36]]. The common-cation rule states that the direct bandgap at the Γ-point of two compound semiconductors with the same cation atom increases as the anion atomic number decreases [46]. Wei *et al.* [36] showed that this can be understood when considering chemical trends (Fig. 2.2) and atomic size contributions. According to the tight-binding model [43], the VBM originates from bonding anion and cation *p* orbitals (InN: In 5*p*, N 2*p*). Because of an increase of the anion *p* orbital energy from N to Sb and enhanced spin-orbit coupling, the energetic position of the VBM in In-group V compounds (InN, InP, InAs, InSb) increases with increasing anion atomic number (Fig. 2.2). The conduction band minimum (CBM) in InN is formed by anti-bonding cation and anion *s* states, i.e., In 5*s* and N 2*s*. The energy of the N 2*s* orbital ($E_{\mathrm{N}2s}$ = -18.5 eV) is very low compared to other group V anion *s* orbital energies (e.g., $E_{\mathrm{P}3s}$ = -14.09 eV). Combined with the effect of a weak deformation potential [$a_{\mathrm{V}}$(InN)=-4.2 eV, $a_{\mathrm{V}}$(InP)=-5.9 eV] which fails to open the bandgap for the case of InN [36], this leads to the exceptionally low position of the CBM with an exceptionally high electron affinity of 5.8 eV [47], and small bandgap.

A direct result of the low CBM in InN is the extremely high position [37, 48, 49] of the branch point or Fermi stabilization energy [49, 50],

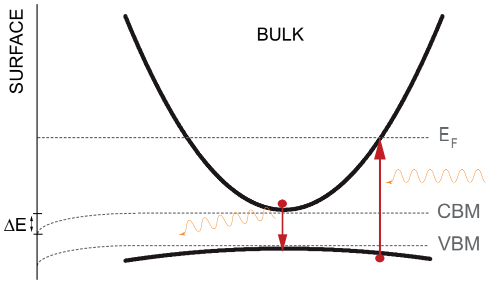

**Figure 2.3.** Schematic illustration of absorption and luminescence properties as well as surface band bending in highly n-type InN with a Fermi energy well above the CBM.

$E_{\mathrm{FS}}$, (Sect. 3.4.2) which is located 1.83 eV above the VBM [37], i.e., ~1.2 eV above the CBM [Fig. 2.2(a)]. This means that for Fermi levels lower than 1.83 eV above the VBM, defects are preferentially incorporated as donors, which explains the strong propensity of InN toward n-type conductivity. While high electron concentrations can be easily achieved via doping with donor impurities or high-energy particle irradiation, InN is very difficult to dope p-type. Additionally, an electron accumulation layer is present at most InN surfaces [19, 51] that complicates the characterization of p-type material. In as-grown InN samples, the surface Fermi energy is located well below the branch point energy. Therefore, unoccupied surface states will preferentially be donor-type and a positively charged surface state area forms. In order to maintain charge neutrality, the surface charge has to be compensated by a downward bending of the conduction band and an increase in the surface electron concentration, i.e., the formation of a surface electron accumulation area (Fig. 2.3). A pinning of the surface Fermi energy at the branch point energy has been observed in slightly n-type samples [37]. Changes in the space charge can be accommodated by slight variations in the surface Fermi energy. With increasing free electron concentration in the bulk, the surface Fermi energy moves significantly closer to the branch point energy to help balance out the surface state charge, and fewer surface states are occupied.

## 2.3 Optical and electrical properties

In low temperature absorption spectra of MBE grown high-quality InN ($n_{\mathrm{e}}$ = mid-$10^{17}$ cm$^{-3}$) [4, 14], strong band edge absorption is measured for energies above $\sim$0.67 eV which coincides with the band-to-band photoluminescence (PL) peak slightly below that energy [4, 14]. For increasing free electron concentrations, a significant blue-shift of the absorption edge is observed. This can be explained [45, 52] by band-filling in the conduction band due to its finite density of states (cf., Burstein-Moss effect [53]). For Fermi energies inside the conduction band, optical absorption from the VBM to the CBM is forbidden and the absorption edge is shifted to: $E_{\mathrm{F}} - E_{\mathrm{V}} > E_{\mathrm{G}}$ (Fig. 2.3). The strength of the Burstein-Moss effect is especially significant in materials with a low density of states in the conduction band and is inversely proportional to the effective mass. Photoluminescence below the Fermi energy is still possible for $E_{\mathrm{F}} > E_{\mathrm{G}}$, but significantly broadened [45].

The small effective mass in InN leads to a high electron mobility, with best samples currently exhibiting values of $\sim$2000 cm$^2$/Vs [54]. The relevance of native defects for the mobility in n-type InN is studied in Ch. 8. Due to the pinning of the Fermi energy at surface states (Fig. 2.3), a distinct electron accumulation layer with sheet densities (i.e., number of carriers per unit area) of up to $N_{\mathrm{S}} = 1.65 \times 10^{13}$ cm$^{-2}$ can be observed at most as-grown InN surfaces [20, 54]. The exploitation of the electron accumulation layer formed at the surface of InN hetero-structures is of high interest for device applications [21, 22].

## 2.4 Defects and doping

InN possesses a strong propensity to n-type conductivity [55] with free electron concentrations in as-grown nominally undoped films ranging from $10^{17}$–$10^{21}$ cm$^{-3}$. The microscopic origin is still under debate and has been investigated extensively [4, 32, 47, 55, 56, 58–66]. Impurities such as H, O and Si are incorporated easily into the InN lattice during common growth processes and act as shallow donors in the material [Fig. 2.4 (a)]. In a recent study, Janotti *et al.* [58] proposed hydrogen ($H_{\mathrm{i}}^{+}, H_{\mathrm{N}}^{2+}$) as the main source of doping in InN. However, it seems that impurities cannot account alone for all the donor concentration [54, 61]. On the side of native

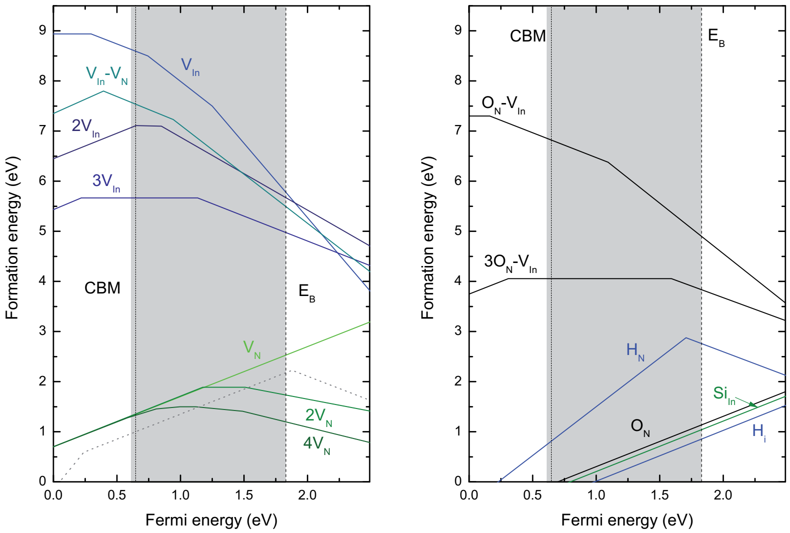

**Figure 2.4.** Calculated formation energies (in case of vacancy complexes: per vacancy) of relevant native defects and impurities as well as their complexes in In-rich InN as a function of the Fermi energy. In case of multiple stable charge states of a defect, only the lowest energy configuration is shown. Kinks in the calculated lines indicate charge transition levels (Eq. 3.3). Data from Refs. [55–57]. For $V_{\mathrm{N}}$ data from two different references are shown (dotted line).

point defects, N vacancies ($V_{\mathrm{N}}^{+/3+}$) [56] are considered the most dominant contributions in bulk. At the interface, contributions from charged dislocation lines [61] have to be considered in addition.

First evidence of successful p-type doping of InN has been published recently [67]. Mg is expected to act as a shallow acceptor in InN [4]. However, the investigation of p-type conductivity in InN is complicated by the strong surface electron accumulation. Density functional theory (DFT) calculations [56, 57] predict that In vacancies ($V_{\mathrm{In}}$) and their complexes are the dominant native acceptor type defects, but their formation energies are high [Fig. 2.4 (b)]. For high Fermi level positions, also $V_{\mathrm{N}}$ and $V_{\mathrm{N}}$ complexes with negative charge states are expected. Acceptor-type defects have been studied extensively in this work and results are presented in Ch. 6–8.

## 2.5 Investigated samples

During the work on this thesis, a variety of different samples has been studied. In the following, a quick overview on their background and prop-

**Table 2.1.** List of samples, including appearance in publication, growth method and possible post-growth treatment, as well as free electron concentrations and mobilities determined from Hall measurements. References to the origin of the samples are included.

| Pub. | Sample | Ref. | $n_e$ ($cm^{-3}$) | $\mu$ ($cm^2/Vs$) |
|---|---|---|---|---|
| I | MBE (Si-doped) | [26] | $1\times10^{18}$ | 1850 |
| I | MBE (Si-doped) | [26] | $2\times10^{18}$ | 1850 |
| I | MBE (Si-doped) | [26] | $1.2\times10^{19}$ | 450 |
| I | MBE (Si-doped) | [26] | $4.8\times10^{19}$ | 100 |
| I, V, VI | MBE (Si-doped) | [37, 68] | $4.5\times10^{19}$ | 600 |
| I, V, VI | MBE (Si-doped) | [37, 68] | $1.3\times10^{20}$ | 150 |
| I, III, VI, V | MBE (Si-doped) | [37, 68] | $4.0\times10^{20}$ | 80 |
| I, V, VI | MBE (Si-doped) | [37, 68] | $6.6\times10^{20}$ | 38 |
| II, V, VI | MBE, He-irr. ($\phi = 8.9\times10^{15}$ $cm^{-2}$) | [60, 69] | $3\times10^{20}$ | 60 |
| II, III,V, VI | MBE, He-irr., RTA | [60, 69] | $6\times10^{19}$ | 400 |
| III | MOCVD | [70, 71] | | |
| IV | MOCVD (T=550°C) | [27] | $4.5\times10^{18}$ | 1070 |
| IV | MOCVD (T=525°C) | [27] | $1.6\times10^{19}$ | 647 |
| IV | MOCVD (T=517°C) | [27] | $1.1\times10^{19}$ | 779 |
| IV | MOCVD (T=500°C) | [27] | $1.3\times10^{19}$ | 536 |

erties is given. Table 2.1 shows a list of most relevant samples that were investigated intensively for Pubs. I–VI.

### 2.5.1 MBE

So far, MBE grown InN represents the highest quality material available in terms of structural, electrical and optical properties. For most of the studies on point defects in InN presented in the following, MBE grown samples were used. State-of-the-art as-grown InN layers, for which no positron annihilation at open volume defects was observed, were used as reference samples for the annihilation state at the InN lattice.

Two sets of Si-doped MBE samples have been investigated in this work. Set I consists of low-doped films with electron concentrations from $1\times10^{18}$ $cm^{-3}$–$4.8\times10^{19}$ $cm^{-3}$ [26], set II includes higher doped films with free electron concentrations from $4.5\times10^{19}$ $cm^{-3}$–$6.6\times10^{20}$ $cm^{-3}$ [37, 68]. All films have been deposited by plasma-assisted molecular beam epitaxy (PAMBE) on c-plane sapphire substrates with a GaN buffer layer [68].

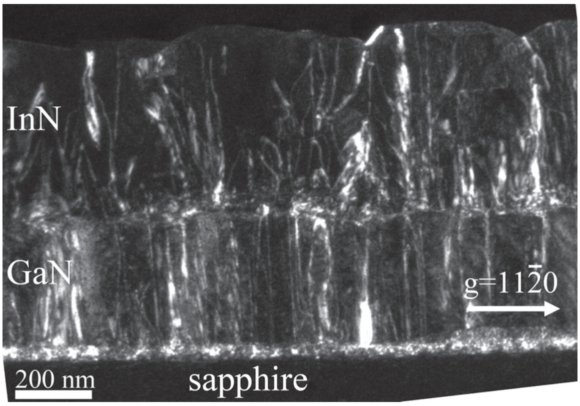

**Figure 2.5.** Cross-sectional TEM micrograph for $g$ = 11-20 of a representative Si-doped sample ($n_e$ = $4.0\times10^{20}$ cm$^{-3}$) grown on sapphire with a GaN buffer layer. Edge and mixed type dislocations are visible (bright features).

Mobilities as determined from single field Hall measurements vary from 38–1850 cm$^2$/Vs. Fig. 2.5 shows the TEM micrograph of the InN film and GaN buffer layer area of a representative Si-doped sample.

Undoped InN films with a thickness of 0.6–2.7 $\mu$m were grown by MBE on c-sapphire substrate with a GaN or AlN buffer layer [60, 65, 69]. The residual electron concentrations and corresponding mobilities ranged between $n_\mathrm{e}$=$6\times10^{17}$–$1\times10^{18}$ cm$^{-3}$ and $1100$–$500$ cm$^2$/Vs, respectively [69]. Irradiation with 2 MeV $^4$He ions was performed at room temperature with fluences of $5.6\times10^{14}$–$1.8\times10^{16}$ cm$^{-2}$, and electron concentrations (mobilities) increased (decreased) up to $5\times10^{20}$ cm$^{-3}$ (down to $\mu = 40$ cm$^2$/Vs) with the highest irradiation fluence. Irradiated samples were further processed by rapid thermal annealing (RTA) at temperatures of 425–475 °C. This showed to significantly improve the mobility while the electron concentration decreased only slightly [69].

### 2.5.2 MOCVD

InN layers were grown by MOCVD in an AIXTRON [72] close coupled showerhead (CCS) reactor on MOCVD GaN-on-sapphire templates. Trimethylindium (TMIn) and ammonia ($NH_3$) were employed as precursors for In and N, and $N_2$ was used as carrier gas. Reactor pressure of 800 mbar and 600 mbar were used, and a V/III ratio of 146k was chosen. The growth temperature was varied from 500–550°C. For more details on the sample growth and properties please see Ref. [27].

# 3. Defects in semiconductors

In this chapter, a basic introduction to the physics and properties of crystalline defects is given. In Sect. 3.1 and Sect. 3.2, defects are classified according to their geometrical configuration and electric properties, respectively. Important defect introduction mechanisms are discussed in Sect. 3.3, and Sect. 3.4 describes basic thermodynamic concepts related to defects in semiconductors. In Sect. 3.5 a short summary of relevant defect characterization methods is presented. A more complete treatment of defects in semiconductors can be found, e.g., in Refs. [73–78].

## 3.1 Structural classification of defects

Defects can be classified according to their geometrical configuration into point defects (0 dimensional) and extended defects (1–3 dimensional). Point defects are usually constrained to one, or at most a few atoms and can be divided into native defects and impurities, as well as their complexes. Impurities are foreign atoms in the lattice of the host material, and can be present either on lattice sites, i.e. substitutional, or interstitial positions. Native defects are formed by mere modifications of the ideal lattice structure. These can be empty lattice sites, i.e. vacancies, or host atoms which are displaced into interstitial positions, i.e. self-interstitials. In the case of compound semiconductors such as InN, also antisite defects can be formed by atoms occupying opposite sub-lattice sites. Frenkel defects are nearby pairs of vacancies and interstitials. Schottky defects are vacancy pairs created by the simultaneous removal of a two opposite atoms in compound semiconductors.

Extended defects include dislocations (1D), stacking faults and grain- or phase boundaries (2D), as well as larger structures such as atomic precipitates or larger voids (vacancy clusters) in the crystal structure (3D). Dislocations can be divided into two extreme cases, i.e., screw and edge-type dislocations. Edge dislocations can be imagined as an extra half-plane of atoms inserted midway through the crystal lattice. To visualize a screw dislocation, a crystal is cut half-way along a lattice plane with one half slipped across the other. Edge and screw dislocations can be identified by their Burgers vector, which represents the magnitude and direction of the lattice distortion connected to the introduction of the dislocation. In edge dislocations, the Burgers vector is normal to the dislocation line direction, in screw dislocations parallel. Dislocations with both parallel and perpendicular component in the burgers vector are mixed dislocations.

Stacking faults and grain- or phase boundaries are the main planar defects. A stacking fault is formed by a spatially limited alteration of the stacking order of the atomic planes. Grain and phase boundaries describe the sudden change of the crystallographic direction or phase. Three-dimensional defects include, e.g., atomic precipitates or larger voids (vacancy clusters) in the crystal structure.

## 3.2 Electrical properties

Modifications in the crystal lattice can lead to changes of a material's electronic properties and the introduction of new defect-related energy states into its band-structure. According to their energetic position with respect to the band edges, defects are often divided into shallow [74, 75] and deep levels [77, 78].

Shallow level defects possess energy levels which are located in the close vicinity of the band edges. If a charge-transfer level from the neutral to the positive (negative) charge state is located close to or above (below) the conduction (valence) band it can act as a major source of free electrons (holes). Shallow level defects are efficient donors (acceptors) and can be introduced intentionally for n- (p-) doping of a semiconductor. They can be described well within the effective mass theory (EMT) as small perturbations of the host band-structure and are mainly derived from the nearest band edges [74, 79]. Their real-space wave function is highly de-localized and the extension in **k**-space is strongly confined. Donor impurity atoms are a good example of this type of defects.

Deep level defects, in contrast, are highly localized defects that constitute severe perturbations of the local electronic structure and induce energy levels deep inside the bandgap. They include many crystal imperfections associated with broken bonds—such as vacancies, surface- and interface reconstructions and other extended defects [74]. Due to their highly localized nature, deep levels do not follow much the movement of the band edges, and hence cannot be described by EMT. Tight-binding as well as first-principle methods have proved useful for the description of deep level defects [77]. Because the energy required to induce transitions from the nearest band edges to the defect state is usually much larger than the thermal energy (25 meV at 300K), deep level defects do not enhance the conductivity. They can act, however, as efficient carrier traps and recombination centers.

## 3.3 Defect introduction

The initial source of defect introduction is the crystal growth process. Defect incorporation during epitaxial growth is governed by a variety of parameters such as growth temperature and kinetics, chemical reactions, lattice mismatch, surface and ambient conditions, as well as material specific properties. Complete control over defect introduction during growth is generally not possible. Apart from the introduction of native defects, semiconductor growth is also almost always a source of material contamination with foreign impurities through, e.g., a contaminated growth chamber or substrate, residues of chemical reactants and impure material sources. Impurities may also be supplied intentionally for doping of a semiconductor. While impurity contamination of a crystal can be limited to some extent by better control over the growth process, this is often not the case for the incorporation of native defects.

Post-growth processing and treatments are important tools for modifying the defect properties of a crystal. These include thermal, chemical and mechanical treatments as well as particle irradiation and implantation. For thermal treatments, a crystal is heated to a desired temperature followed by a rapid or slow cooling procedure (cf., annealing and quenching) [75]. While quenching can be used to fix defect concentrations at a non-equilibrium high temperature value, annealing involves sufficiently low cooling rates to achieve, in theory, crystal perfection as dictated by the lowest reached temperature. In rapid thermal annealing (RTA), crystals are brought to high temperature for a short duration and subsequently cooled down slowly. High energy particle irradiation with, e.g., electrons, protons but also heavier ion sources ($^4_2$He), is a common method for controlled point defect creation in semiconductor crystals. High energy particles passing through a crystal lose their energy mainly by scattering and electronic excitation mechanisms. This creates a defect profile which can be divided into two main areas, i.e., an irradiated area dominated by the creation of Frenkel pairs and an end-of-range area. If the acceleration energy is adjusted so that particles thermalize completely inside the target material, this technique can be used to implant source ions into a host crystal and create well defined doping profiles. Ion implantation is a widely used method in semiconductor device manufacturing.

## 3.4 Thermodynamics of defects

At thermal equilibrium, all defect properties of a material are well-defined and can be determined from thermodynamical considerations [74]. In order for a material to reach thermal equilibrium, sufficient relaxation mechanisms, i.e., opportunities for point defect creation and annihilation, have to be provided [73]. For this, elevated temperatures and high defect mobilities are supportive. Although true thermal equilibrium is hardly ever reached, a partial equilibrium state may be sufficiently close to deduce important defect properties and trends from equilibrium considerations. Thermodynamics can be a very useful tool for discussing defect processes in semiconductors. Nevertheless, extreme care has to be taken when applying thermal equilibrium observations as the properties of real crystals may in practice differ significantly [75].

### 3.4.1 Defect formation energies

At thermal equilibrium, the Gibbs free energy $G$ of a system is defined as the difference between the enthalpy $H$ and the product of absolute temperature $T$ and entropy $S$. The change in Gibbs free energy for the formation of a defect, $\Delta G_{\mathrm{F}}$, in a chemical reaction is given as

$$\Delta G_{\mathrm{f}} = \Delta H_{\mathrm{f}} - T\Delta S_{\mathrm{f}}. \tag{3.1}$$

Here, $H_{\mathrm{f}}$ is the defect formation enthalpy, and $S_{\mathrm{f}}$ the formation entropy. The introduction of defects increases the crystal's enthalpy but also its entropy. Therefore, defects will be formed or annihilated until the thermal equilibrium is reached, i.e., the Gibbs free energy is minimized ($\Delta G_{\mathrm{f}} = 0$). At thermal equilibrium, the concentration of a defect can be calculated as [55, 80]

$$c = N_{\text{conf}} N_{\text{sites}} \exp(-\frac{G_{\mathrm{f}}}{k_{\mathrm{B}}T}) = N_{\text{conf}} N_{\text{sites}} \exp(\frac{S_{\mathrm{f}}}{k_{\mathrm{B}}}) \exp(-\frac{H_{\mathrm{f}}}{k_{\mathrm{B}}T}), \tag{3.2}$$

where $N_{\text{conf}}$ is the number of equivalent configurations for the defect, $N_{\text{sites}}$ the number of available lattice sites per unit volume, and $k_{\mathrm{B}}$ is the Boltzmann constant. For practical calculations using DFT, $G_{\mathrm{f}}$ is often identified with a defect formation energy, $E_{\mathrm{f}}$, that is defined as [80]

$$E_{\mathrm{f}}(X^q) = E_{\text{tot}}(X^q) - E_{\text{tot}}(bulk) - \sum_i n_i \mu_i + q(E_{\mathrm{F}} + E_{\mathrm{V}} + \Delta V). \tag{3.3}$$

Here, $E_{\text{tot}}(X^{\mathrm{q}})$ is the total energy of the supercell containing the defect $X$ in the charge state $q$, $E_{\text{tot}}(bulk)$ the energy of the defect-free bulk cell, $n_i$ is the number of atoms added or removed to create the defect, and $\mu_i$ their chemical potential. $E_{\mathrm{F}}$ and $E_{\mathrm{V}}$ are the energies of the Fermi level and VBM, respectively, and $\Delta V$ is a correction term to align the reference potential of the defect with the bulk supercell. The defect formation energy, $E_{\mathrm{f}}$, defines the equilibrium concentration of a certain defect at a specific temperature; a high formation energy translates to a low defect concentration, and vice versa. For increasing Fermi level, the formation energy of a negatively (positively) charged defect decreases (increases). Therefore, the formation of charged donors (acceptors) is less favorable under n-type (p-type) conditions, but becomes advantageous when approaching p-type (n-type) conductivity. This leads to the concept of self-compensation, i.e., the compensation of dopant-induced free carriers by the formation of native point defects (Ch. 8).

### 3.4.2 Amphoteric defect model and Fermi stabilization energy

Based on the above considerations, a phenomenological model has been developed which proved to be very useful for understanding basic defect-related behavior in various semiconductors. In the amphoteric defect model (ADM) [49, 50], the charge state of so-called amphoteric defects is determined by the position of the Fermi energy with respect to a universal energy reference called the Fermi stabilization energy ($E_{\mathrm{FS}}$). If the Fermi energy is located below (above) $E_{\mathrm{FS}}$, the formation of positive (negative) charge states is energetically favorable.

The Fermi stabilization energy is not correlated to the position of the conduction or valence band edges of a material but is universally located $\sim$4.9 eV below the vacuum level [49]. It marks the Fermi level position at which donor and acceptor type defects are formed at the same rate, and at which the Fermi energy will stabilize as an effect of large introduction of native defects as, e.g., in particle irradiation. Amphoteric defects are, strictly speaking, defects that possess both positive and negative charge states depending on the position of the Fermi energy. Examples of amphoteric defects are the Ga vacancy acceptor and As vacancy donor in GaAs, which transfer to an As antisite plus As vacancy donor [$V_{\mathrm{Ga}}^{3-} + \mathrm{As}_{\mathrm{As}} \leftrightarrow (\mathrm{As}_{\mathrm{Ga}} + V_{\mathrm{As}})^{3+}$], and Ga antisite plus Ga vacancy acceptor [$V_{\mathrm{As}}^{+} + \mathrm{Ga}_{\mathrm{Ga}} \leftrightarrow (\mathrm{Ga}_{\mathrm{As}} + V_{\mathrm{Ga}})^{3-}$], respectively, depending on the position of $E_{\mathrm{F}}$ [50]. The transition from donor to acceptor state occurs at $E_{\mathrm{FS}}$, hence stabilizing the Fermi energy. The Fermi stabilization energy (which is closely related to the branch point energy, or charge neutrality level) was found to serve as a reference for highly localized defects in general, i.e., native defects [49], surface and interface states [81, 82] or transition-metal impurities [83]. Additionally, a similar universal energy alignment has been proposed for the donor-to-acceptor charge transfer level of shallow hydrogen impurities in semiconductors, insulators and solutions [84].

### 3.5 Defect characterization methods

A variety of experimental methods exist for the study of defects in semiconductors [85]. So far, no single characterization method alone can provide a full picture of the nature and properties of defects in a specific sample. In most cases, a combination of several techniques is required for comprehensive characterization of the defect landscape. All defect characterization techniques rely on the measurement of at least one physical property which is linked to the presence of defects in the material. Many fundamental semiconductor properties such as mobility, optical absorption, carrier concentration and lifetime are strongly defect-dependent. Their measurement can provide valuable information on the presence of defects in a specific sample. Beyond this, more specialized defect characterization methods can also provide further detailed defect properties, such as their density, atomic structure, energy levels, charge states and radiative/non-radiative configurations. Positron annihilation spectroscopy has been the main experimental method for the work in this thesis and is especially well-suited for the study of vacancy-type defects. It is presented in more detail in Chs. 4 and 5. Electrical measurements and transmission electron microscopy have been used in Pubs. V and VI. They are briefly introduced below. For a general introduction to experimental defect characterization methods, please consider Refs. [85, 86]. Apart from experimental methods, significant progress in computational approaches for the calculation of material properties using DFT have developed *ab-initio* calculations into a valuable tool for defects studies in semiconductors [80].

Electrical measurements can give access to fundamental properties of a material, such as its resistivity, carrier mobility, concentration and lifetime. Many of these properties are defect dependent and, hence, electrical measurements can be used as indirect defect probes. Hall effect, capacitance-voltage (CV) and current-voltage (IV) measurements belong to the most widely applied electrical characterization methods, together with deep level transient spectroscopy (DLTS) which is a versatile technique for the study of defects with energy levels deep in the bandgap. Specific material requirements, however, may prevent the successful application of the above methods for defect studies. In the case of InN, the electron accumulation layer at most as-grown surfaces [19] has prevented the creation of depletion regions (e.g., by Schottky contacts or *p-n* junctions) — which are a fundamental requirement in CV and DLTS measurements. Ohmic contacts for Hall measurements, on the other hand, can be easily applied on InN surfaces. Hall effect measurements are based on recording the Hall voltage which forms perpendicular to the direction of a current through a sample with the thickness $d$, and an applied external magnetic field. It can be used to determine the type of majority carrier, its sheet density and mobility. Also in Hall measurements, care has to be taken to be able to separate contributions from the bulk and surface of the sample (Ch. 8). This counts especially for thin samples, for which a significant contribution from the surface electron accumulation layer is measured [54].

In scanning electron microscopy (SEM), an electron beam is scanned over the surface of the sample and the electron-beam generated signals such as low-energy secondary electrons, high-energy backscattered electrons or light emitted from the sample, are visualized for each raster point. These signals carry information on the sample topography, composition and luminescence properties and can be recorded with appropriate detectors. SEM is a standard tool for semiconductor characterization, e.g., for the study of sample thicknesses or surface properties. Transmission electron microscopy (TEM) uses the transmitted electrons that undergo different interactions on their way through the sample. For TEM measurements, the preparation of thin sample slices is necessary, e.g., by polishing, etching or ion milling. Bright and dark field images generated from the directly transmitted or the diffracted beams can be used to visualize the crystal structure as well as for the study of extended defects in the material, amongst others.

# 4. Positron annihilation spectroscopy

Positron annihilation spectroscopy (PAS) is a powerful technique for the investigation of defects in semiconductors. In this chapter, an introduction to main aspects of PAS is given. A short summary of important positron interaction mechanisms in semiconductors is presented in Sect 4.1. Two important positron annihilation techniques, Doppler broadening spectroscopy and positron lifetime spectroscopy, are introduced in Sects. 4.2 and 4.3, respectively. Computational approaches in positron annihilation spectroscopy are presented separately in Sect. 5.2. For more details on PAS please consider, e.g., Refs. [9–12] and references therein.

## 4.1 Theory of positrons in semiconductors

The positron ($e^+$) is the antiparticle of the electron, and as such carries the same spin and mass as the electron, but opposite charge. Its existence has been first postulated by Dirac [87] in 1928 and experimentally discovered in 1932 by Anderson [88], for which the latter received the Nobel Prize in Physics in 1936.

When an energetic positron hits a crystal, it thermalizes quickly and starts diffusing through the lattice where it eventually can get trapped at a defect site and annihilates with a crystal electron (Fig 4.1). This annihilation process occurs mainly through the emission of two 0.511 MeV $\gamma$-photons in nearly opposite directions that carry away energy and momentum of the annihilating $e^+$-$e^-$ pair. Thermalization times in semiconductors are usually very short, of the order of a few ps, and energy loss is mediated mainly through ionic scattering and electron-hole pair generation. For energies lower than the bandgap of the material, phonon scattering becomes relevant. The diffusion length $L_+$ is a function of the

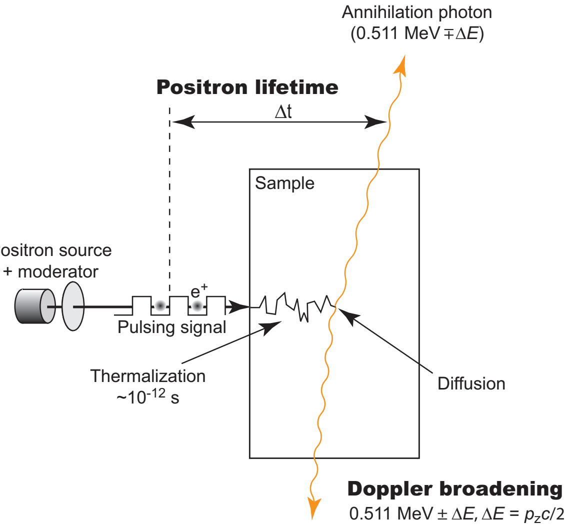

**Figure 4.1.** Schematic illustration of different positron annihilation experiments using a slow-positron beam. Monoenergetic positrons from a positron source are implanted into a crystal where they thermalize quickly and diffuse through the lattice. Before annihilating with a crystal electron they can get trapped at defect sites. This affects the positron lifetime and line-shape of the Doppler broadened 0.511 MeV $\gamma$-radiation emitted by annihilating e-p pairs. Measurement of the positron lifetime and line-shape of the emitted annihilation radiation reveals important information about the physical properties at the annihilation site.

positron lifetime $\tau$ and the diffusion constant $D_+$,

$$L_+ = \sqrt{\tau D_+}, \quad \text{with} \quad D_+ = \tau_\mathrm{r}\frac{k_\mathrm{B}T}{m_+^*}, \tag{4.1}$$

where $\tau_\mathrm{r}$ is the relaxation time of the dominant scattering mechanism and $m_+^*$ the positron effective mass.

In the presence of defects the positron diffusion length can be significantly reduced due to positron trapping at defects. This is caused by a reduction of the effective positron lifetime in the lattice:

$$\tau_\mathrm{eff} = 1/(\lambda_\mathrm{b} + \kappa), \quad \text{with} \quad \lambda_\mathrm{b} = \frac{1}{\tau_\mathrm{b}}. \tag{4.2}$$

Here, $\tau_\mathrm{b}$ is the positron lifetime, $\lambda_\mathrm{b}$ the positron annihilation rate in defect-free bulk, and $\kappa$ is the defect-specific positron trapping rate. The positron lifetime, $\tau$, and its inverse, the positron annihilation rate, $\lambda$, can be calculated from the overlap of electron and positron densities during annihilation (Eq. 5.17, Sect. 5.2). Typical positron lifetimes in defect-free semiconductors are in the range of ~150–300 ps. Positron lifetimes for trapped states at open-volume defects are longer.

The positron trapping rate at a crystal defect, $\kappa$, is proportional to the positron trapping coefficient, $\mu$, and the defect density, $\rho$,

$$\kappa = \mu\rho. \tag{4.3}$$

Positron trapping coefficients have been calculated for monovacancies in silicon by Puska *et al.* [10] and room-temperature values range from $4\times10^{14}$ s$^{-1}$, for the neutral charge state, to $2.5\times10^{15}$ s$^{-1}$ for the negatively charged case. For negatively charged defects, the positron trapping coefficient increases at low temperatures proportional to $T^{-1/2}$ and reaches $5\times10^{16}$ s$^{-1}$ at 5 K. This is due to the formation of extended shallow Rydberg states around the defect site, which trap positrons efficiently at low temperatures. Due to their low positron binding energy $E_\mathrm{b}$ of only ~10–100 meV, de-trapping from these states has to be considered. The de-trapping rate $\delta_\mathrm{st}$ is given as

$$\delta_\mathrm{st} = \frac{\kappa_\mathrm{st}}{\rho_\mathrm{st}}(\frac{m_+^* k_\mathrm{B}T}{2\pi\hbar^2})^{3/2}\exp(\frac{E_\mathrm{b}}{k_\mathrm{B}T}). \tag{4.4}$$

For the case of negatively charged vacancy defects, the de-trapping rate from these states is usually small compared to the transition rate to the deep vacancy state. However, in case no deep bound state exists, e.g., for negatively charged non-open volume defects, de-trapping becomes relevant.

In the general case of *n* different positron trapping defects, the positron annihilation fractions at the *i*-th defect ($\eta_i$) and the bulk ($\eta_\mathrm{b}$) can be calculated with

$$\eta_\mathrm{b} = \frac{\lambda_\mathrm{b}}{\lambda_\mathrm{b} + \sum_{i=1}^{\mathrm{n}}\kappa_i^\mathrm{eff}},\ \eta_i = \frac{\kappa_i^\mathrm{eff}}{\lambda_\mathrm{b} + \sum_{i=1}^{n}\kappa_i^\mathrm{eff}}. \tag{4.5}$$

The effective trapping rate for the *i*-th defect, $\kappa_i^\mathrm{eff}$, is defined for the general case, including de-trapping with the rate $\delta_i$ (Eq. 4.4), as

$$\kappa_i^\mathrm{eff} = \frac{\kappa_i}{1 + \delta_i/\lambda_i}, \tag{4.6}$$

and $\kappa_i^\mathrm{eff}$ equals $\kappa_i$ for $\delta_i = 0$.

Although bound positron states might also exist for positive vacancies, the room-temperature trapping rate to positively charged vacancies is typically much smaller than the positron annihilation rate. Hence, positively charged vacancy defects are usually not observed in positron annihilation spectroscopy.

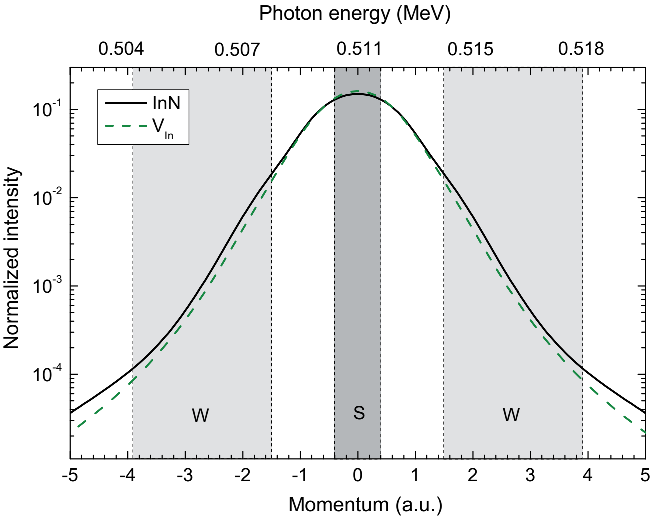

**Figure 4.2.** Calculated line-shape of the Doppler-broadened 511 keV $\gamma$-radiation emitted by annihilating electron-positron pairs in the delocalized state of the InN lattice, and trapped at an In vacancy in InN, respectively (Sects. 5.2, 6.2). The momentum of annihilating e-p pairs is displayed in atomic units. S and W parameters are commonly used to describe the peak line-shape via the fractional counts in the low and high-momentum area, respectively.

## 4.2 Doppler broadening spectroscopy

In the electron-positron (e-p) annihilation process, the energy of the emitted $\gamma$-radiation is Doppler shifted by the center of mass of electron and positron momentum. While the positron can be considered completely thermalized, the electron momentum is significant. The energy shift $\Delta E$ caused by the component of the electron momentum $p$ in detection direction $z$ is

$$\Delta E = \frac{1}{2} c p_z. \tag{4.7}$$

Due to the distribution of electron momenta, a broadening of the annihilation line-shape is observed when recording multiple annihilation events. The shape of the annihilation line, $L(E_\gamma)$, is given by the one-dimensional momentum distribution of the annihilating e-p pair,

$$L(E_\gamma) \propto \int\int dp_x dp_y \rho(\mathbf{p}); \quad p_z = \frac{2}{c}\Delta E_\gamma \tag{4.8}$$

For positrons annihilating in the trapped state at an open volume defect, the line-shape of the annihilation spectrum narrows due to an increased annihilation fraction with low-momentum valence electrons, and a decrease in high-momentum core electron annihilations (Fig. 4.2). The measured annihilation spectrum is characteristic for a certain annihilation state and can also be calculated with DFT (Sect. 5.2). Hence, Doppler broadening spectroscopy can be used for the chemical identification of annihilation states.

Energy sensitive high-purity Ge-detectors are used for recording the annihilation $\gamma$-radiation. The full-width-at-half-maximum (FWHM) of the Gaussian detector resolution function of $\sim$1.3 keV (at 0.511 MeV) is in the range of the typical line width of the annihilation radiation (2–3 keV). Therefore, a large number number of events ($\sim 1\times 10^6$) has to be recorded to ensure statistical reliability. Instead of looking at the complete spectrum, line-shape parameters are often employed to analyze the Doppler broadening. The commonly used S and W parameters (Fig. 4.2) characterize the relative counts in the low and high momentum areas of the spectrum, respectively, with usual integration windows of $|p_L(S)| < 0.4$ a.u. ($\Delta E_\gamma < 0.75$ keV) and 1.5 a.u.$< |p_L(W)| < 3.9$ a.u. (2.9 keV $< \Delta E_\gamma < 7.3$ keV). For improvement of the spectra, measurements can be performed in the coincidence mode [89, 90] where both annihilation photons are detected simultaneously and only counted if energy conservation is fulfilled ($E_{\mathrm{tot}}$ = 1.022 MeV). This improves the peak-to-background ratio up to $10^6$ and sharpens the detector resolution, which is especially required when analyzing the full annihilation spectrum rather then using the line-shape parameters.

In positron annihilation experiments the time-integrated annihilation parameter $P$ (e.g., average positron lifetime, annihilation line-shape, S and W parameter) is a superposition of the characteristic values of present positron traps $P_i$ and the crystal lattice $P_{\mathrm{b}}$, weighted with the positron annihilation fractions at the lattice ($\eta_{\mathrm{b}}$) and the $i$-th defect ($\eta_i$), respectively,

$$P = \eta_{\mathrm{b}} P_{\mathrm{b}} + \Sigma_{i=1}^{\mathrm{n}} \eta_i P_i, \quad \text{with} \quad \eta_{\mathrm{b}} = 1 - \Sigma_{i=1}^{\mathrm{n}} \eta_i. \tag{4.9}$$

For a well-known set of characteristic parameters ($P_i$, $P_{\mathrm{b}}$, $\lambda_{\mathrm{b}}$), Eq.4.9 can be used together with Eqs. (4.5) and (4.3), to determine the positron trapping rate and density of a specific defect from the measured annihilation parameters:

$$\kappa_i^{\mathrm{eff}} = \lambda_{\mathrm{b}} \frac{P - P_{\mathrm{b}}}{P_i - P} + \sum_{j\neq i}^{n} \kappa_j^{\mathrm{eff}} \frac{P - P_j}{P_i - P} = \mu_i \rho_i. \tag{4.10}$$

While the experimental determination of defect trapping rates is straightforward for the case of only one dominant vacancy-type positron trap, the situation is significantly complicated for several types of different traps. Characteristic parameters of both defects and bulk can be determined through measurement of representative samples with a well-defined defect structure and comparison with positron lifetime experiments (Sect. 4.3). Additionally, DFT calculations of positron lifetimes and momentum density spectra, as presented in Sect. 5.2, can be a powerful tool in this context.

## 4.3 Positron lifetime spectroscopy

In positron lifetime spectroscopy, the time difference between the birth and the annihilation of a positron is measured. The experimental positron lifetime spectrum $N(t)$,

$$N(t) = I_\mathrm{b} e^{-\lambda_\mathrm{b} t} + \sum_{i=1}^{n} I_i e^{-\lambda_i t}, \tag{4.11}$$

is the probability distribution of positrons annihilating at the time $t$ and derived from solving the set of differential equations describing annihilation in the defect-free bulk state and $n$ defects [9]. One main advantage of positron lifetime spectroscopy is that the different lifetime components and, hence, defect trapping rates $\kappa_i$ can be directly determined by decomposition of the exponential decay spectrum in Eq. 4.11 [9],

$$\kappa_i = I_i(\lambda_\mathrm{b} - \lambda_i) \tag{4.12}$$

An important experimental quantity is the average positron lifetime $\tau_\mathrm{ave}$ which is defined as the center of mass of the positron lifetime spectrum,

$$\tau_\mathrm{ave} = \frac{I_\mathrm{b}}{\lambda_\mathrm{b}} + \sum_{i=1}^{n} \frac{I_i}{\lambda_i} = I_\mathrm{b}\tau_\mathrm{b} + \sum_{i=1}^{n} I_i \tau_i. \tag{4.13}$$

While the decomposition of measured spectra can be considered reliable only up to 3 decay components, the average lifetime can be determined with high accuracy (<1 ps) independently of the number of trapping centers. Using $\tau_\mathrm{ave}$ as the annihilation parameter in Eq. 4.10, an additional important method for the estimation of trapping rates is supplied.

The time resolution of common positron lifetime setups is in the range of $\sim$200–250 ps (FWHM) and mainly determined by the choice of detectors, for which fast scintillators coupled to photomultiplier tubes are usually used. This limits the determination of lifetimes to components longer than 50 ps [9].

## 4.4 Positron sources and beams

Experimental positron sources can be divided into two main classes, i.e., laboratory-scale sources using radioactive isotopes which decay through the $\beta^+$-mode, and sources utilizing positron generation through pair-production. Positrons from pair-production are mainly available as a by-product in large scale user facilities, and the $\gamma$-radiation can stem from, e.g., bremsstrahlung or nuclear reactions. The $\beta^+$-isotope $^{22}$Na decays to $^{22}$Ne through the reaction

$$^{22}\mathrm{Na} \;\rightarrow\; ^{22}\mathrm{Ne} + \mathrm{p} + \nu_\mathrm{e} + \gamma, \tag{4.14}$$

under the emission of a positron, electron neutrino ($\nu_\mathrm{e}$) and a $\gamma$-quantum of 1.27 MeV. The almost simultaneous emission of positron and $\gamma$-quantum, which can be used as a convenient start-signal in positron lifetime experiments, as well as the high positron yield [9] of 90.4% make $^{22}$Na the most commonly used laboratory source. Due to the energy contribution of the electron neutrino, the energy spectrum of positrons emitted in the $\beta^+$-decay is continuous with a maximum energy of 0.545 MeV. This leads to a broad positron implantation profile into an adjacent solid with a mean implantation depth of, e.g., 40 $\mu$m in GaN [91].

If a specific depth inside a material should be probed, the supply of monoenergetic positrons with well-defined kinetic energies is necessary. This is realized in slow-positron beams by moderation of energetic positrons to room-temperature and subsequent acceleration by an electric field. In that way, an energy range from several tens of eV to several tens of keV is accessible. Common moderators consist of a thin foil of material with negative positron work function (e.g., tungsten) in which a certain fraction of energetic positrons get first thermalized and then spontaneously re-emitted from the surface. The construction of slow-positron beams for positron lifetime experiments is additionally complicated by the lack of an obvious start signal. One method to overcome this challenge is bunching of the positron beam [92].

The implantation profile of monoenergetic positrons with the energy $E$ in a solid has a Makhovian profile of the form [9, 93]

$$P(x,E) = \frac{m x^{m-1}}{x_0^m} e^{-(\frac{x}{x_0})^m}, \;\; \text{with } x_0 = \frac{AE^r}{\rho\Gamma(1+\frac{1}{m})}. \tag{4.15}$$

Here, $m$ = 2, $r$ = 1.6 and $A$ = 4.0 $\mu$g cm$^{-2}$ keV$^{-r}$ are widely used empirical parameters [9, 94], $\Gamma$ is the gamma function and $\rho$ the mass density of the material. The mean positron implantation depth is given as

$$\bar{x} = AE^r/\rho. \tag{4.16}$$

Calculated implantation profiles and mean implantation depths for InN are shown in Fig. 6.4 for representative positron implantation energies. Depth-dependent defect profiles can be determined from energy-dependent measurements of a positron annihilation parameter by solving the one-dimensional positron diffusion equation under consideration of the positron implantation profile as, e.g., implemented in the fitting tool VEPFIT developed by van Veen *et al.* [95].

# 5. Computational approach to electron and positron states in semiconductors

Electronic structure calculations using density functional theory (DFT) methods are a powerful tool for *ab-initio* modeling of ground-state properties of semiconductors and have found wide application in materials research [96], e.g., for the study of defects in InN [55–58, 64, 80, 84, 97]. Section 5.1 presents a short introduction to the basic concepts of DFT calculations.

DFT calculations have been used extensively in Pub. III for the investigation of positron annihilation properties of vacancy defects in InN (Ch. 6). The integration of positrons into electronic structure calculations is accomplished in the framework of the two-component density functional theory [10, 11, 90, 98–101] and is introduced in Sect. 5.2.

## 5.1 Electronic structure calculations

The time-independent many-body Schrödinger equation for $N$ electrons in an external potential $\hat{V}$ is written in the Born-Oppenheimer approximation as [96]:

$$\hat{H}\Psi = [\hat{T} + \hat{V} + \hat{U}]\Psi = [\sum_{i}^{N}(-\frac{\hbar^2}{2m}\nabla_i^2) + \sum_{i}^{N} V(\mathbf{r}_i) + \sum_{i<j}^{N} U(\mathbf{r}_i, \mathbf{r}_j)]\Psi \qquad (5.1)$$
$$= E\Psi$$

where $\hat{\mathrm{H}}$ is the electronic Hamilton operator, $\hat{\mathrm{T}}$ the kinetic energy and $\hat{\mathrm{U}}$ the electron-electron interaction energy. In practice, it is impossible to solve Eq. 5.1 for more than a few electrons.

Instead of solving Eq. 5.1 directly, DFT follows an alternative approach which is summarized in the Hohenberg-Kohn theorem [102]. It states that the ground state properties of an $N$-electron system are uniquely determined by an electronic density $n(\mathbf{r})$ which can be derived by finding the global minimum of the functional $E_{\mathrm{HK}}$,

$$E_{\mathrm{HK}}[n] = T[n] + E_{\mathrm{int}}[n] + \int d\mathbf{r}\, V_{\mathrm{ext}}(\mathbf{r})n(\mathbf{r}) + E_{\mathrm{II}}, \tag{5.2}$$

with $T[n]$ the kinetic energy, $E_{\mathrm{int}}$ the electronic and $E_{\mathrm{II}}$ the ionic interaction energy. For any external potential $V_{\mathrm{ext}}$, this energy minimum is equal to the ground state energy of the studied system.

The Kohn-Sham ansatz [103] offers a way of solving Eq. 5.2 by analogy to a system of non-interacting particles with the same electron density $n$,

$$E_{\mathrm{KS}}[n] = T_{\mathrm{s}}[n] + \frac{1}{2}\int d\mathbf{r}d\mathbf{r'}\, \frac{n(\mathbf{r})n(\mathbf{r'})}{|\mathbf{r}-\mathbf{r'}|} + \int d\mathbf{r}\, V_{\mathrm{ext}}(\mathbf{r})n(\mathbf{r}) + E_{\mathrm{II}} + E_{\mathrm{XC}}[n], \tag{5.3}$$

where $T_{\mathrm{s}}[n]$ is the kinetic energy of a system of noninteracting electrons with the density $n$. $E_{\mathrm{XC}}[n]$ is the exchange and correlation term which includes the difference in kinetic energy between the non-interacting model system and Eq. 5.2 as well as all possible many-particle interactions,

$$E_{\mathrm{XC}}[n] = T[n] - T_{\mathrm{s}}[n] - \frac{1}{2}\int d\mathbf{r}d\mathbf{r'} \frac{n(\mathbf{r})n(\mathbf{r'})}{|\mathbf{r}-\mathbf{r'}|} + E_{\mathrm{int}}[n]. \tag{5.4}$$

One of the most common expressions for $E_{\mathrm{XC}}$ is given with the local density approximation (LDA). Here, the energy contribution of each volume element is replaced by the energy equivalent of a homogeneous electron gas of the same density at that point ($\varepsilon_{\mathrm{XC}}^{\mathrm{hom}}$),

$$E_{\mathrm{XC}}^{\mathrm{LDA}} = \int d\mathbf{r}\varepsilon_{\mathrm{XC}}^{\mathrm{hom}}(n(\mathbf{r}))n(\mathbf{r}). \tag{5.5}$$

The $N$ single electron Schrödinger equations in the Kohn-Sham approximation can be written as

$$-\frac{1}{2}\nabla^2\psi_i(\mathbf{r}) + V_{\mathrm{eff}}(\mathbf{r})\psi_i(\mathbf{r}) = \varepsilon_i\psi_i(\mathbf{r}), \tag{5.6}$$

with the effective potential

$$V_{\mathrm{eff}}(\mathbf{r}) = \int d\mathbf{r}\, \frac{n(\mathbf{r})}{|\mathbf{r}-\mathbf{r}'|} + V_{\mathrm{ext}}(\mathbf{r}) + \frac{\delta E_{\mathrm{XC}}[n]}{\delta n(\mathbf{r})}, \tag{5.7}$$

where $\frac{\delta E_{\mathrm{XC}}[n]}{\delta n(\mathbf{r})}$ is the exchange and correlation potential. The electron density $n(\mathbf{r})$ can be calculated by summation over all occupied single-particle wavefunctions $\psi_i$ in Eq. 5.6,

$$n(\mathbf{r}) = \sum_{i=1}^{N} |\psi_i(\mathbf{r})|^2, \tag{5.8}$$

and its converged value is found by minimization of the energy in Eq. 5.3.

## 5.2 Calculation of positron states and parameters

A possibility for integration of positrons into DFT calculations has been introduced by Boroński and Nieminen [100] with the two-component density functional theory (TCDFT). Here, the total energy functional in Eq. 5.3 is generalized to include both positron ($n_+$) and electron density ($n_-$),

$$\begin{aligned} E[n_-, n_+] =& F[n_-] + F[n_+] - \int d\mathbf{r}d\mathbf{r'}\, \frac{n_-(\mathbf{r})n_+(\mathbf{r'})}{|\mathbf{r}-\mathbf{r'}|} \\ &+ \int d\mathbf{r}\, V_{\text{ext}}(\mathbf{r})[n_-(\mathbf{r}) - n_+(\mathbf{r})] + E_{\text{co}}^{\text{e-p}}[n_-, n_+], \end{aligned} \tag{5.9}$$

where $E_{\text{co}}^{\text{e-p}}[n_-, n_+]$ is the electron-positron correlation-energy functional and $F[n_*]$ the single component functional for electrons or positrons,

$$F[n_*] = T[n_*] + \frac{1}{2}\int d\mathbf{r}d\mathbf{r'} \frac{n_*(\mathbf{r})n_*(\mathbf{r'})}{|\mathbf{r}-\mathbf{r'}|} + E_{\text{XC}}[n_*]. \tag{5.10}$$

This leads to the following set of modified Kohn-Sham equations:

$$-\frac{1}{2}\nabla^2\psi_i^-(\mathbf{r}) + V_{\text{eff}}^-(\mathbf{r})\psi_i^- = \varepsilon_i^-\psi_i^-(\mathbf{r}), \tag{5.11}$$

$$-\frac{1}{2}\nabla^2\psi_i^+(\mathbf{r}) + V_{\text{eff}}^+(\mathbf{r})\psi_i^+ = \varepsilon_i^+\psi_i^+(\mathbf{r}). \tag{5.12}$$

The effective potentials $V_{\text{eff}}^-(\mathbf{r})$ and $V_{\text{eff}}^+(\mathbf{r})$ are expressed as

$$V_{\text{eff}}^-(\mathbf{r}) = -\phi(\mathbf{r}) + \frac{\delta E_{\text{XC}}[n_-]}{\delta n_-(\mathbf{r})} + \frac{\delta E_{\text{co}}^{\text{e-p}}[n_+, n_-]}{\delta n_-(\mathbf{r})}, \tag{5.13}$$

$$V_{\text{eff}}^+(\mathbf{r}) = \phi(\mathbf{r}) + \frac{\delta E_{\text{XC}}[n_+]}{\delta n_+(\mathbf{r})} + \frac{\delta E_{\text{co}}^{\text{e-p}}[n_+, n_-]}{\delta n_+(\mathbf{r})}, \tag{5.14}$$

with the total Coulomb potential

$$\phi(\mathbf{r}) = \int d\mathbf{r'}\, \frac{-n_-(\mathbf{r'}) + n_+(\mathbf{r'})}{|\mathbf{r}-\mathbf{r'}|} - V_{\text{ext}}(\mathbf{r})[n_-(\mathbf{r}) - n_+(\mathbf{r})]. \tag{5.15}$$

The densities of electrons and positrons can be calculated similarly to Eq. 5.8 by summation over all occupied wavefunctions.

The electron-positron correlation functional $E_{\text{co}}^{\text{e-p}}[n_+, n_-]$ in Eq. 5.9 is badly known for finite positron densities. A common approximation is the so-called conventional scheme which assumes that the positron does not influence the average electron density. Additionally, the enhancement and electron-positron correlation functionals are evaluated in the zero-positron density limit ($n_+ \rightarrow 0$). This is only exact for the case of a completely delocalized positron in the crystal lattice (bulk), but can be also justified for finite positron densities localized at a defect site when considering the positron and its screening cloud as a neutral quasi-particle which does not influence the average electron density. In this scheme, the electron density is first calculated independently and then the positron state (Eq. 5.12) is solved in the potential

$$V_+(\mathbf{r}) = -\int d\mathbf{r'}\,\frac{n_-(\mathbf{r'})}{|\mathbf{r}-\mathbf{r'}|} - V_{\text{ext}}(\mathbf{r}) + V_{\text{corr}}(n_-(\mathbf{r})), \tag{5.16}$$

i.e., the sum of the attractive Hartree potential due to electrons, the external potential due to the nuclei, and $V_{\text{corr}}(n_-(\mathbf{r}))$, the electron-positron correlation potential at the $n_+ \to 0$ limit. For the latter, the Boronski-Nieminen parametrization can be used [100].

The positron annihilation rate can be calculated as

$$\lambda = \frac{1}{\tau} = \pi r_{\text{e}}^2 c \int d\mathbf{r} n_+(\mathbf{r}) n_-(\mathbf{r}) \gamma(n_-(\mathbf{r})), \tag{5.17}$$

where $\gamma(n_-(\mathbf{r}))$ is an enhancement factor which accounts for the increased electron-positron contact density due to the screening, solved in the zero-positron limit within the LDA [100].

In order to calculate the momentum distribution of annihilating electron-positron pairs, further approximations have to be made. The approximation $\gamma(n_-(\mathbf{r})) = 1$ is called the independent particle model. In the state-dependent scheme by Alatalo *et al.* [90], an electron-state dependent but position and momentum-independent enhancement factor is used,

$$\gamma_j = \frac{\lambda_j^{\text{(BN-LDA)}}}{\lambda_j^{\text{(IPM)}}}. \tag{5.18}$$

Here, $\lambda_j^{\text{(BN-LDA)}}$ is the Boronski-Nieminen parametrized [100] annihilation rate in the LDA,

$$\lambda_j^{\text{(BN-LDA)}} = \pi r_{\text{e}}^2 c \int d\mathbf{r}\;\; n_+(\mathbf{r}) |\psi_j(\mathbf{r})|^2 \gamma(n_-(\mathbf{r})), \tag{5.19}$$

and $\lambda_j^{\text{(IPM)}}$ is the annihilation rate for $\gamma$=1. In this approximation, the momentum density of annihilating electron-positron pairs is written as

$$\rho(\mathbf{p}) = \pi r_{\text{e}}^2 c \sum_j \gamma_j \left| \int d\mathbf{r} e^{-i\mathbf{pr}} \psi_+(\mathbf{r}) \psi_j(\mathbf{r}) \right|^2. \tag{5.20}$$

# 6. Identification of dominant vacancy-type positron traps in InN

Early positron annihilation studies of InN found considerable trapping of positrons at open volume defects in as-grown material deposited by MBE [104, 105] and MOCVD [70], as well as irradiated [65] and Si-doped samples [106, 107]. Comparison with simple atomic superposition calculations [98] of the positron lifetime and electron-positron momentum distribution identified the positron traps in early MBE-grown films as In-sublattice related vacancies [104, 105]. However, the exact chemical identity of these defects remained unknown. Further studies indicated the presence of several types of positron traps in different areas and samples (Pubs. I, II).

In Pub. III, a comprehensive search of potential vacancy-type positron traps in InN was performed using state-of-the-art density functional theory methods [101]. Calculated positron annihilation parameters (Sect. 6.2) of energetically favorable vacancy defects and complexes (Sect. 6.1) are compared to positron lifetime (Pubs. I, II) and high-resolution Doppler broadening spectra (Pub. II) of several representative InN samples in order to identify the dominant vacancy-type positron traps in common InN material.

## 6.1 Computational details

Positron trapping and annihilation properties for a selection of isolated vacancies ($V_{\mathrm{In}}$, $V_{\mathrm{N}}$), mixed (n$V_{\mathrm{In}}$-m$V_{\mathrm{N}}$) and pure vacancy clusters (n$V_{\mathrm{In}}$, m$V_{\mathrm{N}}$) and vacancy-impurity complexes ($V_{\mathrm{In}}$-n$O_{\mathrm{N}}$, $V_{\mathrm{In}}$-$Si_{\mathrm{In}}$) in InN have been investigated using density functional theory calculations. The selection of defect structures was motivated by previous experimental evidence [108] and DFT calculations (Fig. 2.4). Calculations have been performed applying the conventional scheme in the framework of the two-component density functional theory (Sect. 5.2), i.e., the positron density is assumed not to influence the system's average electron density, and the zero-positron density limit of the enhancement and electron-positron correlation energy functionals are used.

Electronic structure calculations were performed using a 96-atom InN wurtzite supercell, and valence electron densities were calculated self-consistently using the local density approximation (LDA) and projector augmented-wave method (PAW) [109] implemented in the VASP code [110]. All defects were calculated in the neutral charge state. Details on the construction of the defect supercells can be found in Pub. III. Ionic positions were relaxed with a convergence criterium of 0.01 eV/Å for forces. Indium 4d electrons were treated as valence and an energy cut-off of 400 eV was chosen. The Brillouin zone was sampled with a $3\times3$ Monkhorst-Pack $\mathbf{k}$-point mesh. The positron density was solved independently in the calculated Coulomb potential due to electrons and nuclei and the e-p correlation potential (Eq. 5.16). Subsequently, the positron annihilation rate and lifetime (Eq. 5.19) and the momentum distribution of annihilating e-p pairs (Eq. 5.20) were calculated in the state-dependent scheme [90] (Sect. 5.2). For comparing the calculated 3D momentum density to 1D experimental spectra, the calculated spectra were integrated over the wurtzite $m$-plane and convoluted with a Gaussian of 0.53 a.u. and 0.66 a.u. FWHM, respectively, to simulate the experimental resolution function in coincidence and conventional Doppler measurements. The S and W line shape parameters were calculated from the spectra convoluted with 0.66 a.u. FWHM using integration windows as mentioned in Sect. 4.2.

## 6.2 Computational results

The optimized lattice constants for wurtzite InN are calculated as $a = 3.510$ Å, $c/a = 1.610$ and $u = 0.379$, in good agreement with literature [17, 57]. The positron density in the InN lattice is fully delocalized [Fig. 6.1 (a)], and a positron lifetime of 157 ps is obtained. The difference to the experimental lifetime value [105] of $\sim$180 ps stems from using the LDA enhancement factor. The choice of the LDA is motivated by our focus on the calculation of momentum distributions [101]. In this approx-

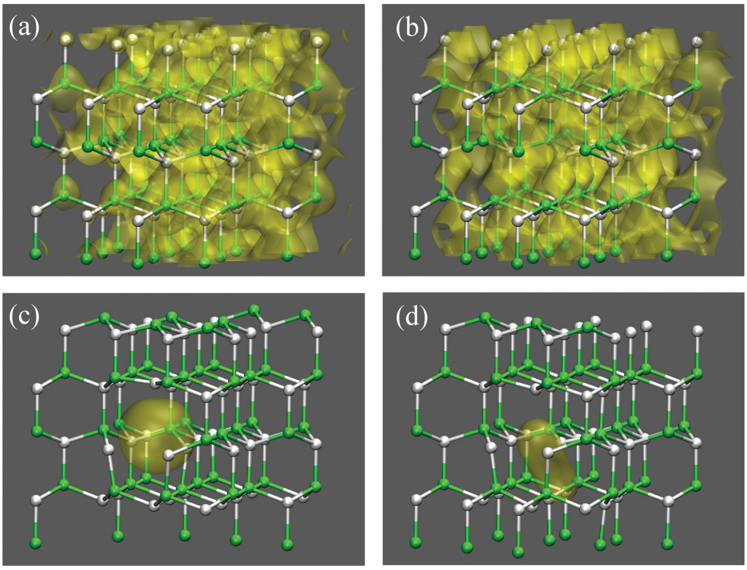

**Figure 6.1.** Isosurface plot of the calculated positron density (transparent sphere) in the relaxed lattice structure of bulk InN (a), and supercells containing a $4V_{\mathrm{N}}$ (b), $V_{\mathrm{In}}$ (c) and $2V_{\mathrm{In}}$ (d) defect. Silver (light) and green (dark) balls indicate N and In ions, respectively.

imation, good agreement with experiments is achieved [101] for positron lifetime differences, $\Delta\tau = \tau_{\mathrm{defect}} - \tau_{\mathrm{bulk}}$, rather than absolute values.

The calculation of the positron state in the defect supercells shows that isolated $V_{\mathrm{N}}$ and pure $V_{\mathrm{N}}$ complexes in the neutral or positive charge state do not localize the positron density. Isolated $V_{\mathrm{In}}$, on the other hand, are efficient positron traps in InN. This remains the case for all calculated defect complexes which include at least one $V_{\mathrm{In}}$. The calculated positron lifetime difference of the $V_{\mathrm{In}}$ to the InN lattice is 85 ps, which is in good agreement with the $\sim$ 80 ps observed in experiments [105, 107]. Positron lifetimes for most of the remaining In-vacancy related defect complexes are very similar with lifetime differences of $\Delta\tau = 85$–$95$ ps. Only for the case of the larger $2V_{\mathrm{In}}$-$V_{\mathrm{N}}$ and $V_{\mathrm{In}}$-$3V_{\mathrm{N}}$ complexes, lifetimes are higher with 109 and 99 ps difference to the InN lattice, respectively. Therefore, positron lifetime measurements are suitable to detect the presence of vacancy defects in InN, but can not be used to distinguish between different vacancy-type positron traps.

Figure 6.2 displays the calculated momentum density spectra of the investigated vacancy structures. The spectra are shown as ratio curves, for which the raw calculated defect momentum density distributions

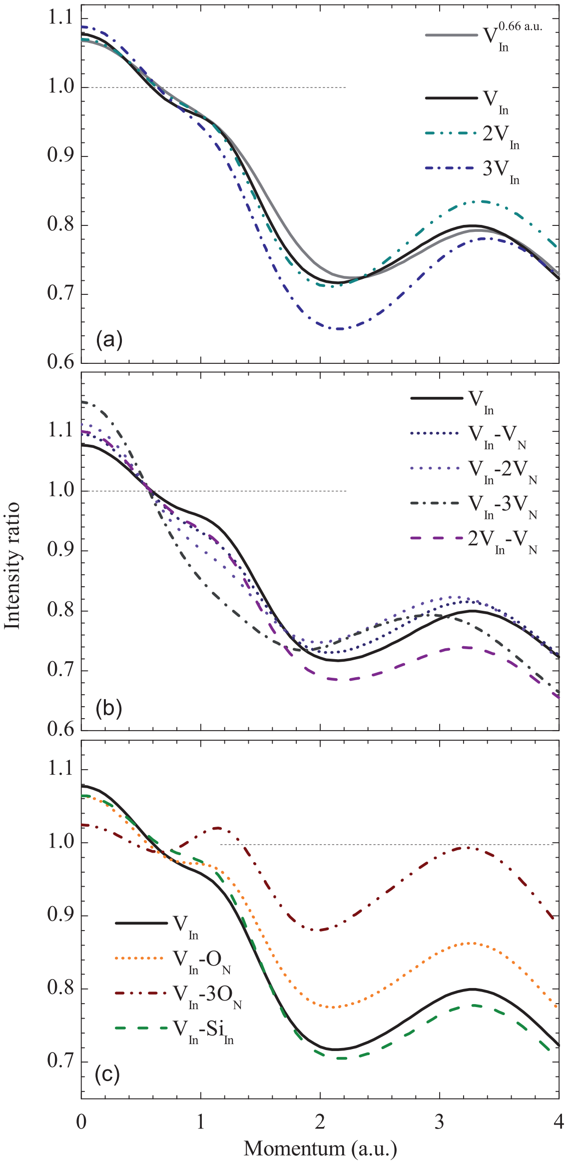

**Figure 6.2.** Ratio curves of the calculated momentum densities of annihilating e-p pairs in selected vacancy complexes in InN. All spectra are convoluted with a Gaussian of 0.53 a.u. FWHM (except $V_{\mathrm{In}}^{0.66\text{ a.u.}}$, FWHM = 0.66 a.u.) and divided by the momentum density spectrum of the InN lattice.

(Fig. 4.2) were folded at the center (0 a.u.) and divided by the spectrum for the defect-free InN lattice in order to accentuate the defect-induced changes. The ratio curve for the $V_{\mathrm{In}}$ [Fig. 6.2 (a)] exhibits a distinct line shape with a maximum of roughly 1.08 at the peak center region (0 a.u.). For momenta above 0.6 a.u. the spectrum drops below 1 and an articulate shoulder is visible at 1.2 a.u. At around 3.3 a.u. a second broad peak appears with an intensity of around 0.8 relative to the InN lattice. For the $2V_{\mathrm{In}}$ complex, a slight increase of the peak at 3.3 a.u. is visible but the absolute intensity at these momentum values is already reduced by $\sim 10^3$ compared to the peak maximum and discrimination (in experiments) is hence considerably complicated. For the $3V_{\mathrm{In}}$, the ratio curve changes significantly with an increased peak maximum and a more pronounced drop at 2.1 a.u. However, the overall line-shape is still very similar to the $V_{\mathrm{In}}$ and $2V_{\mathrm{In}}$.

Fig. 6.2 (b) shows the computed ratio curves of mixed n$V_{\mathrm{In}}$-m$V_{\mathrm{N}}$ complexes. A systematic trend compared to the isolated $V_{\mathrm{In}}$ is visible in the spectra when adding an increasing number of $V_{\mathrm{N}}$ around a single $V_{\mathrm{In}}$. A strong increase of the zero momentum maximum to over 1.15 for the $V_{\mathrm{In}}$-$3V_{\mathrm{N}}$ is visible which is related to the increase in open volume. At the same time, the intensity of the shoulder at 1.2 a.u. decreases with increasing number of $V_{\mathrm{N}}$ until it entirely disappears for the $V_{\mathrm{In}}$-$3V_{\mathrm{N}}$. The ratio curve of the $2V_{\mathrm{In}}$-$V_{\mathrm{N}}$ is close to the $V_{\mathrm{In}}$-$V_{\mathrm{N}}$ for lower momentum values but starts to deviate at around 1.4 a.u. with lower intensities at higher momenta.

The ratio curves of In vacancy-impurity complexes are shown in Fig. 6.2 (c). For $V_{\mathrm{In}}$-$O_{\mathrm{N}}$ complexes, the peak maximum decreases with increasing number of O ions while the intensity in the spectral range above 0.9 a.u. increases, including the shoulder at 1.2 a.u. and the peak at 3.4 a.u. The form of the $V_{\mathrm{In}}$-$O_{\mathrm{N}}$ ratio curve is close to the $V_{\mathrm{In}}$ and resembles a case of $V_{\mathrm{In}}$ trapping with reduced annihilation fraction of $\eta \approx 0.8$. The spectrum of the $V_{\mathrm{In}}$-$Si_{\mathrm{In}}$ is very similar to the $V_{\mathrm{In}}$ and hence hardly distinguishable in experiments. The case is different for the ratio curve of the $V_{\mathrm{In}}$-$3O_{\mathrm{N}}$ which possesses distinct features with the shoulders at 1.2 and 3.6 a.u., respectively, that should be identifiable in coincidence Doppler measurements.

The calculated S and W line-shape parameters for the modeled defect structures are shown in Fig. 6.3. All parameters are normalized to the

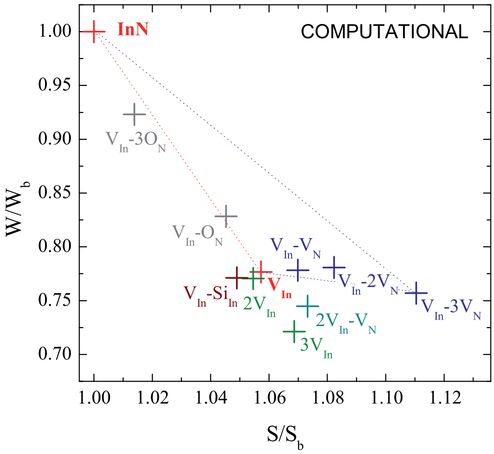

**Figure 6.3.** Calculated S and W line-shape parameters for $V_{\mathrm{In}}$ and complexes in InN. Line-shape parameters were determined from calculated defect spectra which were convoluted with a Gaussian with 0.66 a.u. FWHM, using conventional energy windows (Sect. 4.2). All parameters have been divided by the respective value for the InN bulk.

InN bulk. For the $V_{\mathrm{In}}$, characteristic parameters of S = 1.057 and W = 0.78 are obtained. The $2V_{\mathrm{In}}$ point lies very close to this value. The $3V_{\mathrm{In}}$ complex is located on an extension of the InN -$V_{\mathrm{In}}$ line, i.e., in case of annihilation fractions below $\eta \sim 0.8$ it can not be distinguished from isolated $V_{\mathrm{In}}$. For the $V_{\mathrm{In}}$-m$O_{\mathrm{N}}$ complexes, the situation is comparable. Their position in the SW plot can be reproduced by a reduced annihilation fraction at the isolated $V_{\mathrm{In}}$. Therefore, a distinction between pure $V_{\mathrm{In}}$ and $V_{\mathrm{In}}$-impurity complexes based on their S and W parameters is difficult. For the case of mixed n$V_{\mathrm{In}}$-m$V_{\mathrm{N}}$ complexes, however, a clear deviation from the $V_{\mathrm{In}}$-InN line is visible. For an increasing number of $V_{\mathrm{N}}$ in the vacancy complex, its S parameter increases with only minor changes in the W parameter, hence causing the observed deviation. This leads to clearly different slopes for the $V_{\mathrm{In}}$ - InN, and ($V_{\mathrm{In}}$-m$V_{\mathrm{N}}$) -InN lines.

## 6.3 Doppler broadening and positron lifetime measurements

In order to identify the dominant positron traps in common InN material, positron annihilation measurements were performed on a selection of representative as-grown and irradiated InN layers grown by different growth methods. Three samples are studied in more detail and are presented in Table 6.1. Sample I is MBE-grown material [65] which has been irradiated with 2 MeV He ions to a fluence of $8.9\times10^{15}$ cm$^{-2}$, the remaining samples are as-grown. Sample II is a Si-doped InN layer deposited by MBE [68], sample III has been grown by MOCVD [70, 71] . All samples were deposited as ~500 nm thick layers on sapphire substrates. For samples I and II a GaN buffer layer has been grown between the substrate and the InN layer. Further details on the growth and characteristics of the samples can be found elsewhere [65, 68, 70, 71, 107, 111].

Depth-dependent Doppler broadening spectra (Pubs. I, II, V) show a strong profile in the recorded line-shape parameters from near-surface to the near-interface area for sample I and sample II. A similar profile has been observed in depth-dependent measurements of the average positron lifetime (Ref. [111] and Pub. I). In sample III, no such profile is found and a constant line-shape parameter is measured for the entire layer area of the sample. Figure 6.4 (a) shows the measured S-parameters of sample II for positron implantation energies from 0–20 keV. After annihilation at surface-specific states for low implantation energies, the S-parameter drops quickly to a local minimum at ~6 keV. Comparison with the positron implantation profile (Eq. 4.15) at this energy [Fig. 6.4 (b)] reveals that this point is representative for annihilations from the first 150nm of the sample, with a mean implantation depth of $\bar{x}$=100nm. Deeper inside the sample, the S-parameter increases to a local maximum at ~12 keV (corresponding to a mean implantation depth of $\bar{x}$=310nm) and positrons probe a wide region reaching the interface to the GaN buffer layer. For higher implantation energies a significant number of positrons annihilate in the GaN buffer layer pulling the measured S-parameter towards the value of the GaN lattice. The solid curve in Fig. 6.4 (a) shows a fit of the measured spectrum using the multi-layer fitting program VEPFIT [95]. It reveals that the experimental spectrum can be well described assuming a two-layer structure of the S-parameter inside the InN film (see dashed line)

**Table 6.1.** Studied samples and experimentally determined line-shape parameters of the respective dominant positron trap. All parameters are extrapolated to saturation trapping and divided by the reference values measured in InN lattice.

| | | Layer: | | Interface: | |
|---|---|---|---|---|---|
| **ID** | **Sample** | **$S/S_{ref}$** | **$W/W_{ref}$** | **$S/S_{ref}$** | **$W/W_{ref}$** |
| I | MBE, irr. | 1.042 | 0.80 | 1.083 | 0.78 |
| II | MBE, Si-doped | 1.051 | 0.83 | 1.077 | 0.81 |
| III | MOCVD | 1.052 | 0.81 | / | / |

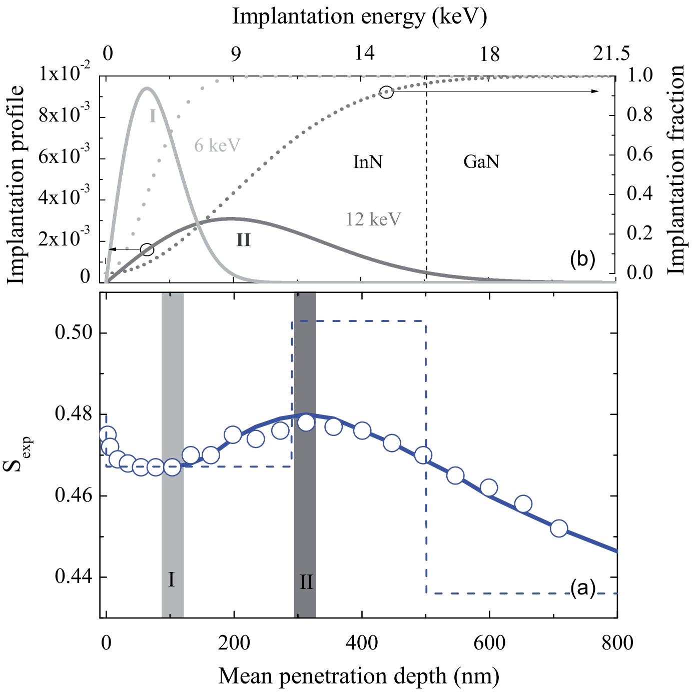

**Figure 6.4.** Measured S parameter (open circles) of sample II as a function of the mean positron implantation depth (a). Corresponding implantation energies are given for comparison. The solid line shows a fit of the data using a simple three-layer model of the S-parameter (dashed line). Figure (b) shows the calculated positron implantation profiles and fractions for positron implantation energies of 6 keV (I) and 12 keV (II).

with a 300 nm thick near-surface and 200 nm thick near-interface layer and a positron diffusion length of ∼5 nm.

Representative for the near-surface ("Layer") and near-interface ("Interface") areas of the sample, the measured S and W parameters at $\bar{x}$=100 nm (6 keV) and $\bar{x}$=310nm (12 keV) are plotted as open symbols in Fig. 6.5. Line shape parameters for sample I have been determined accordingly (Pub. II). Sample III does not exhibit any depth-profile in the line shape parameters and hence only one set of parameters is displayed. All samples were measured perpendicular to the *c*-axis and determined parameters are normalized with the value of an InN reference sample for which no positron trapping to open volume defects is observed [112].

Positron lifetime measurements of sample I [113] and II (Pub. I) showed an increase of the average positron lifetime from the near-surface to near-interface area, similar as observed in Doppler broadening spectra. A decomposition of the lifetime spectrum yields two dominant components,

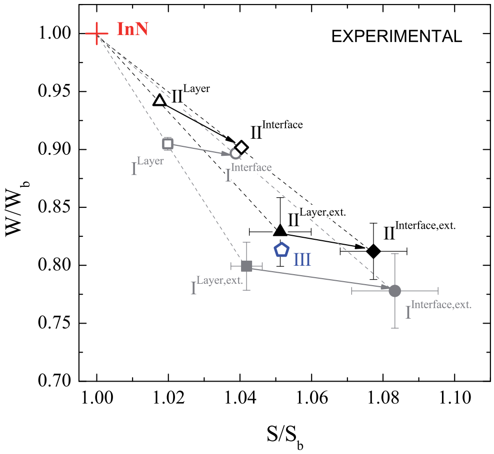

**Figure 6.5.** Experimentally determined S and W values from a conventional Doppler broadening setup for different samples (Table 6.1). Open symbols correspond to directly measured values, closed symbols have been extrapolated using trapping fractions estimated from positron lifetime measurements. Different symbols are used for different samples.

$\tau_1 = 184$ ps and $\tau_2 = 260$ ps. The first component, $\tau_1$, is in good agreement with earlier measured values for the InN lattice [105]. The lifetime difference $\Delta(\tau_2 - \tau_1)$ coincides within the margin of error with the calculated value for the $V_{\mathrm{In}}$ and smaller vacancy complexes in InN. Close to the interface a longer lifetime component contributes to the spectrum, yet only with an intensity of a few percent. Based on the positron lifetime spectra, the positron annihilation fractions at the dominant vacancy defects for the "Layer" and "Interface" points of samples I and II were estimated as $\eta_{\mathrm{I,Layer}} = 0.47$, $\eta_{\mathrm{II,Layer}} = 0.34$, $\eta_{\mathrm{I,Interface}} = 0.47$ and $\eta_{\mathrm{II,Interface}} = 0.52$, respectively. The determined annihilation fractions could be used to extrapolate the measured S and W parameter of samples I and II to saturation trapping (Fig. 6.5, closed symbols).

Figure 6.6 shows the ratio curves of annihilating electron-positron pairs at the dominant open-volume positron traps in the layer (and interface) region of samples I, II and III, as measured using the coincidence Doppler technique (Sect. 4.2). The recorded momentum distributions for samples I and II were again extrapolated to saturation trapping using the above annihilation fractions. When comparing the experimental ratio curve in the layer region of sample I to the calculated momentum distributions in section 6.1, we find good agreement with the spectrum of the isolated $V_{\mathrm{In}}$. In the central region of the peak slightly higher intensities are found in the calculated spectrum compared to the experimental one. This re-

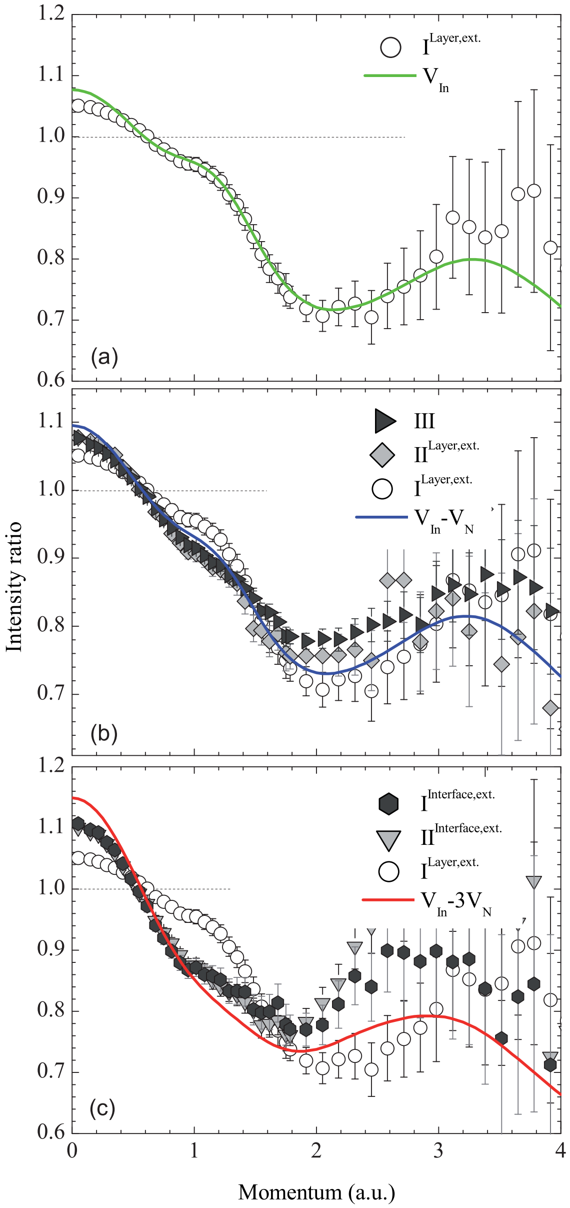

**Figure 6.6.** Experimental coincidence Doppler spectra of the investigated samples in the layer (a,b) and interface (c) region. The data have been divided by a suitable reference spectrum for the InN lattice. Computational ratio curves are shown for comparison.

gion is mostly sensitive to the size of the open volume of the positron trap, with higher intensities for larger volumes. The calculated $2V_{\mathrm{In}}$ and $V_{\mathrm{In}}$-$O_{\mathrm{N}}$ complexes possess an overall rather similar shape of the ratio curve and based on this also have to be considered as possible sources of the defect signal. Nevertheless, the available lifetime data do not support the reduced annihilation fraction which would be required for an identification of the experimental spectrum with the $V_{\mathrm{In}}$-$O_{\mathrm{N}}$. Although the differences between the $V_{\mathrm{In}}$ and $2V_{\mathrm{In}}$ complex are more subtle and hence the $2V_{\mathrm{In}}$ cannot be ruled out as a contribution to the signal, the ratio curve of $V_{\mathrm{In}}$ gives the best overall approximation of the experimental spectrum. Therefore we identify the positron trap created in irradiated InN with the isolated $V_{\mathrm{In}}$.

Compared to sample I, the as-grown samples II and III show several differences in their ratio curves. First, the intensity in the peak center region is clearly increased. The intensity difference to the InN lattice is thereby magnified by about 35 % compared to the spectrum of sample I. This is supported by very accurate statistics in this spectral region. Second, a significant decrease of the shoulder at 1.2 a.u. is visible, also with high statistical accuracy. Third, the drop at 2 a.u. is less pronounced, followed by slightly higher intensities in the high momentum region of the spectrum. Nevertheless, stronger scatter starts to dominate this region. A comparison with the calculated defect spectra in Sect. 6.1 reveals that these changes coincide with the effects of the decoration of a $V_{\mathrm{In}}$ by $V_{\mathrm{N}}$, as presented in Fig. 6.2 (b). Especially the characteristic decrease of the shoulder at 1.2 a.u. in the experimental ratio curve cannot be correlated with any other calculated vacancy defect complex (see additionally Hautakangas *et al.* [114]). This is also expressed in the observed deviation of the characteristic line-shape parameters of sample II and III from the line determined by the characteristic points of sample I and the InN lattice in Fig. 6.5. A similar trend can be observed for the calculated $V_{\mathrm{In}}$-$nV_{\mathrm{N}}$ parameters in Fig. 6.3. Judging from the intensity of the observed changes in the ratio plots an identification of the experimental spectra with $V_{\mathrm{In}}$-$V_{\mathrm{N}}$ is most feasible, with possible influence from the $V_{\mathrm{In}}$-$2V_{\mathrm{N}}$. This assignment is in good agreement with the positron lifetime data [107].

A strong change in the Doppler broadening signal is observed for sample I and II close to the interface region, as visible in Fig. 6.5. In both samples a strong increase in the peak center intensity to about 1.12 is visible, which is over 2-fold compared to that observed in the irradiated layer. Additionally, the signal drops straight to the minimum at 2 a.u. without showing anymore the shoulder which is visible in the layer region of both samples. The observed trends are qualitatively very similar to the ones described in the previous section for the layer region of samples II and III, but intensified. Therefore, we identify the induced changes with an increase in the decoration of $V_{\mathrm{In}}$ with $V_{\mathrm{N}}$. When comparing to calculated momentum distributions, the best agreement is found for the spectrum of the $V_{\mathrm{In}}$-$3V_{\mathrm{N}}$ complex. Results from both conventional Doppler broadening (Fig. 6.5) and positron lifetime spectroscopy additionally support this assignment [107, 113].

Based on the above data, the dominant positron traps created in high-energy particle irradiation of MBE grown InN layers are identified as isolated $V_{\mathrm{In}}$, while in as-grown MBE and MOCVD material the observed defect is a mixed $V_{\mathrm{In}}$-$V_{\mathrm{N}}$ vacancy complex. The changes at the interface of both irradiated material and as-grown layers are assigned to the formation of larger $V_{\mathrm{In}}$-$nV_{\mathrm{N}}$ complexes with an average of about 3 $V_{\mathrm{N}}$ surrounding the $V_{\mathrm{In}}$.

# 7. Vacancy formation and evolution

In Ch. 6, the dominant vacancy type positron traps in common InN material have been identified. In the following, their formation mechanisms and evolution upon different treatments and sample conditions, and dependence on different growth methods and parameters is investigated.

Section 7.1 focuses on InN layers deposited by MBE. In state-of-the-art MBE-grown material with low free electron concentrations the density of $V_{\mathrm{In}}$-related defects is found to be at or below the detection limit of positron annihilation techniques. As-grown InN can be turned highly n-type using, e.g., Si-doping (Sect. 7.1.2) or high-energy particle irradiation (Sect. 7.1.1). In n-type layers, trapping to open-volume positron traps is found to increase with the free electron concentration. Additional effects were encountered at layer/substrate interfaces. A study of the interplay of vacancies and extended defects at interfaces is presented in Sect. 7.1.3.

While MBE techniques are suitable for the growth of highest-quality layers, MOCVD growth does possess strong advantages in terms of industrial applicability. Although strong improvements have been made in recent years [27, 30], the quality of MOCVD grown InN remained still somewhat inferior with carrier concentrations in the mid-$10^{18}$ cm$^{-3}$, about one magnitude larger than in state-of-the-art PA-MBE grown InN material [4, 115]. In Sect. 7.2, the point defect landscape in MOCVD grown layers is investigated with focus on the growth temperature as critical parameter during MOCVD growth.

## 7.1 MBE growth

State-of-the-art as-grown InN layers deposited by MBE can exhibit free electron concentrations as low as $\sim 10^{17}$ cm$^{-3}$ [4]. In these layers, III-

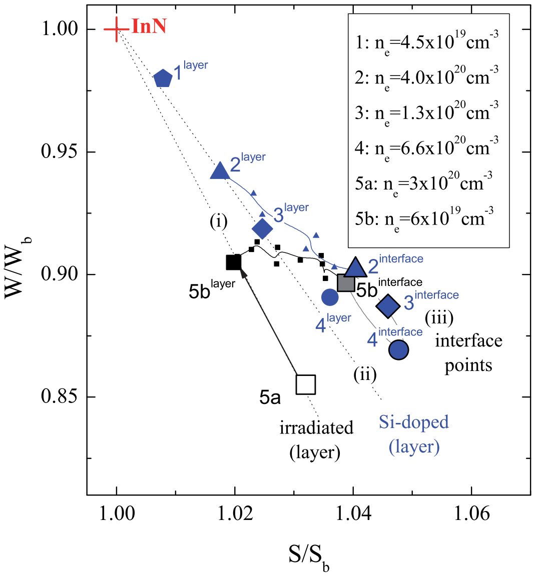

**Figure 7.1.** S and W line-shape parameters of the Doppler broadened e-p $\gamma$-annihilation radiation for different samples and areas.

sublattice related vacancy defects have been found to be at or below the detection limit of positron annihilation spectroscopy, i.e., in the $10^{16}$ cm$^{-3}$ range [111]. This can be understood considering the high position of the Fermi-stabilization energy deep inside the conduction band of the material (Sect. 2.2) and the predominantly negative charge state of $V_{\mathrm{In}}$-related defects in InN (Sect. 2.4). The formation of acceptor type point defects should be unfavorable in low conductivity material. However, the experimentally observed defect concentrations are still by magnitudes higher than those corresponding to calculated formation energies of $V_{\mathrm{In}}$ and its complexes in InN (Sect. 2.4). In Eq. 3.2, a vacancy concentration of $10^{16}$ cm$^{-3}$ requires a formation energy of $\sim$1 eV when assuming a growth temperature of 550°C. In spite of this, theoretical formation energies of $V_{\mathrm{In}}$-related defects in InN are at least 3 eV (which translates to defect concentrations of $< 10^4$ cm$^{-3}$), even in highly n-type conditions. This large discrepancy between experimental and theoretical vacancy concentrations suggests that point defect properties in InN are far away from thermal equilibrium and, hence, alternative defect formation mechanisms dictate the defect concentrations in available InN material. This could be partly explained (Sect.3.4) by the low temperature applied in InN growth compared to, e.g., the growth of GaN. For GaN, growth temperatures are at least 200–300° higher and experimental vacancy concentrations are found to agree well with results from DFT calculations [116]. Additionally, an underestimation of calculated defect formation energies in InN should not be ruled out.

Recent results [111] suggest that limited diffusion of surface adatoms during MBE growth could play a major role in determining the In vacancy related defect concentration in high-quality material. Moreover, a strong correlation between the layer thickness and $V_{\mathrm{In}}$ concentrations [105], as well as the observed enhanced vacancy formation close to the layer-substrate interface (Pub. V) suggest that interface-related phenomena are important factors.

### 7.1.1 Irradiation and annealing

High-energy particle irradiation is an effective way to control the conductivity of undoped InN [69]. Irradiation with 2 MeV $^4He^+$ ions was found to introduce native donors with an electron production rate of $\sim$4$\times10^4$ cm$^{-1}$ until saturation of the free electron concentration at $\sim$4$\times10^{20}$ cm$^{-3}$ [69] (Fig. 8.3), and the mobility was shown to decrease with the electron concentration (Ch. 8). According to earlier work with positron annihilation spectroscopy [65], acceptor type defects are introduced at much lower rates of $\sim$100 and 2000 cm$^{-1}$ for vacancy and negative-ion type defects, respectively. After rapid thermal annealing (RTA) at temperatures ranging from 425 to 475°C, the mobility significantly improved with only small changes in the electron concentration [69].

Doppler broadening spectroscopy has been used to study the point defect landscape in MBE-grown 2 MeV $^4He^+$-irradiated InN layers after RTA. Fig. 7.1 shows the measured line-shape parameter of a representative sample irradiated with a fluence of $\phi$ = 8.9$\times10^{15}$ cm$^{-2}$ before [65] and after RTA at 475°C [111]. All points are normalized with the value of an InN reference sample for which no positron trapping to open volume defects is observed [112]. In the as-grown layer, the measured line-shape parameters are close to the value of the InN bulk [65]. After irradiation with a fluence of $\phi$ = 8.9$\times10^{15}$ cm$^{-2}$, an increase in positron trapping at open-volume defects is detected and a constant line-shape parameter (5a) of $S = 1.020$ and $W = 0.90$ relative to the InN lattice is measured throughout the whole InN layer. Upon RTA [69], a profile in the depth dependent spectrum of the S-parameter is developed for the investigated set of samples [111], with a minimum close to the InN surface, for low positron implantation energies (“layer”), and a maximum for higher energies (“interface”) when a considerable number of positrons is annihilating near the interface with the GaN buffer layer (cf. Sect. 6.3). The "layer" point remains on the same line defined by the as-irradiated sample, but is shifted closer toward the lattice point. This indicates an unchanged identity of the dominant irradiation-induced positron trap but a decrease of the annihilation fraction. In Ch. 6, the dominant open volume positron trap in the layer region of the irradiated sample has been identified as the isolated $V_{\mathrm{In}}$. The "interface" point is shifted to higher S-values with only minor changes in the W parameter. This indicates a change in the identity of the dominant vacancy-type positron trap near the interface, which could be identified as complexing of the $V_{\mathrm{In}}$ with approximately 2–3 $V_{\mathrm{N}}$ (Ch. 6). The observed re-arrangement of vacancy defects near the interface is supported by TEM measurements where an increased density of dislocation loops is observed after RTA, possibly resulting from an agglomeration of irradiation-induced vacancy defects [69, 117].

It can be concluded that high-energy particle irradiation introduces isolated $V_{\mathrm{In}}$ as dominant vacancy-type positron traps. Subsequent annealing leads to a re-arrangement of vacancies [111]. $V_{\mathrm{In}}$ become mobile at or below the annealing temperature and start to move toward the surface or the interface with the GaN buffer where they either recombine, anneal out (at the surface) or form complexes with residual $V_{\mathrm{N}}$ (interface). Assuming a jump rate of 1 $\mathrm{s}^{-1}$ and diffusion coefficient $D_0 = 10^{13} s^{-1}$ [118] , an upper limit of $E_{\mathrm{b}} \leq$ 1.9 eV for the migration barrier of the $V_{\mathrm{In}}$ can be estimated, based on an annealing temperature of T $\leq$ 475°C. This is in good agreement with the calculated value of 1.6 eV [57] and indicates that isolated $V_{\mathrm{In}}$ are mobile during InN growth at the usual growth temperatures of $\sim 550°$C for MBE.

### 7.1.2 Si-doping

Si on the In lattice site ($\mathrm{Si}_{In}$) is an effective n-dopant in InN [4, 37, 56]. In Pubs. I, V and VI, Si-doped InN layers with free electron concentrations of $1\times10^{18}$–$6.6\times10^{20}$ $\mathrm{cm}^{-3}$ have been investigated. All samples were deposited as ~500 nm thick layers on sapphire substrates with a GaN buffer layer of ~200 nm. For more details on the sample properties, please see

Sect. 2.5.

Figure 7.1 shows the measured line-shape S and W parameters at the “Layer” and “Interface”' points (Sect. 6.3) for a selection of Si-doped samples with free electron concentrations of mid-$10^{19}$ $cm^{-3}$ and above. All points have been divided by the characteristic value of a suitable reference sample for the InN lattice where no positron trapping to open volume defects is observed. Measured line-shape parameters for lower-doped samples are close to the characteristic point for the InN lattice (Pub. I) and omitted in the figure. For samples 1 - 4, all "layer" points fall on one line through the characteristic point of the InN reference sample. Hence [12], one dominant vacancy-type positron trap is present, which could be identified in Ch. 6 as the $V_{\mathrm{In}}$-$V_{\mathrm{N}}$ complex. No isolated $V_{\mathrm{In}}$ are observed in the measurements of as-grown Si-doped InN. Therefore we conclude that in InN, in-grown $V_{\mathrm{In}}$ are stabilized through the formation of complexes with $V_{\mathrm{N}}$. This is supported by recent DFT results [57] that predict a positive binding energy between $V_{\mathrm{In}}$ and $V_{\mathrm{N}}$. Vacancy-stabilization through the formation of vacancy-donor complexes has been observed also in GaN (see [119] and the references therein) and AlN [120]. With increasing free electron concentration from $4.5\times10^{19}$ $cm^{-3}$ to $6.6\times10^{20}$ $cm^{-3}$ , the measured S (W) parameter increases (decreases) which indicates an increasing positron annihilation fraction at the vacancy complexes from sample 1 to 4. At room temperature, the measured layer S parameter of sample 2 is lower than the determined value in sample 3, hence, not obeying that trend. Measurements at high temperature, however, were found to reverse the order (Ch. 8).

For the "interface" points, an increase in the S-parameter and deviation from the "layer" line is observed for samples 2–4 due to less pronounced changes in the W-parameter. This coincides with the changes observed at the interface of the irradiated samples after annealing (Sect. 7.1.1) and could be explained with increased decoration of the $V_{\mathrm{In}}$-$V_{\mathrm{N}}$ complexes by $V_{\mathrm{N}}$ (Ch. 6). The observation of enhanced formation of larger $V_{\mathrm{In}}$-$nV_{\mathrm{N}}$ complexes toward the interface with the GaN buffer layer in both irradiated material after annealing, as well as Si-doped samples, indicates that the interface acts as a sink for vacancy defects. An agglomeration of both $V_{\mathrm{In}}$ and $V_{\mathrm{N}}$ in that area is necessary to provide the required proximity of defects for the promotion of vacancy clustering. Duan *et al.* have calculated [64] for n-type conditions a positive binding energy between single

$V_N$ and a strong tendency for the formation of larger $V_N$ clusters. Hence, the formation of the observed $V_{In}$-$nV_N$ complexes at the interface could occur through a precursor state of $nV_N + V_{In} \rightarrow V_{In}$-$nV_N$, as proposed also for Mg-doped InN [121].

### 7.1.3 Interaction between vacancies and extended defects

InN has a large lattice mismatch with common substrate and buffer materials, e.g., 10%, 13% and 25% for c-plane GaN, AlN and sapphire, respectively [5]. Therefore, a large number of strain releasing dislocations (Ch. 3) are expected to form at the interface between the InN layer and the buffer/ substrate. In order to investigate the interaction between the formation of point and extended defects at InN interfaces, transmission electron microscopy (TEM) measurements of the Si-doped and irradiated samples were performed (Pub. V). Figure 2.5 shows a cross-sectional TEM micrograph obtained in weak beam (WB) conditions with a reciprocal lattice vector of $g$ = 11-20 for a representative Si-doped sample. Edge and mixed type dislocations are visible distributed throughout the InN layer with an average density of $4.0\times10^9$ cm$^{-2}$ and $1.1\times10^9$ cm$^{-2}$, respectively. An agglomeration of dislocations close to the InN/GaN interface can be noticed. The density of screw type dislocations is $3.1\times10^8$ cm$^{-2}$ which corresponds to $\sim$6% of the total dislocation density. Additionally, a high density ($3\times10^5$ cm$^{-1}$) of stacking faults was revealed in WB conditions [122] with $g$ = 10-10 (not shown here). In the irradiated InN film, earlier TEM results [117] showed irradiation induced creation of dislocation loops, additional to planar defects introduced during growth. After annealing at 475 °C the density of dislocation loops increased from $2.2\times10^{10}$ cm$^{-2}$ to $9.0\times10^{10}$ cm$^{-2}$ [69, 117]. Vacancy agglomeration after annealing was proposed to be the reason for this increase.

The observed increase in vacancy clustering at the InN/Gan interface coincides with elevated dislocation densities in that area. In order to assess whether the strain field in the vicinity of dislocations could affect the formation energy of point defects we performed DFT calculations of strained InN bulk cells. We found that typical strain associated with screw dislocations (0–15% shear) decreases the formation energies of $V_{In}$ and $V_N$ only slightly by $\leq$30 meV, and hence should not play any major role. Comprehensive theoretical calculations including the effect of edge dislocations will be published elsewhere [123]. However, besides strain-related influences on the defect formation energies, dislocation movement and/or decoration of dislocations should also be considered as possible dislocation related vacancy formation mechanisms. To the best of our knowledge, no direct correlation between dislocation densities and vacancy concentrations in InN could be established so far [62, 115]. This is in contrast to GaN where vacancy concentrations and dislocation densities tend to be correlated [124]. Recent results by Kraeusel *et al.* [125] indicate that stable dislocation cores including vacancies also exist in InN. It should be noted that the presence of dislocations might also directly affect the positron annihilation signal [126] and it has been suggested that dislocations act as shallow traps for positrons. Exceptionally low values for the positron diffusion length in the InN samples do indicate the presence of additional positron trapping centers with annihilation characteristics close to the bulk [127]. Calculations on positron trapping and annihilation at dislocations in wurtzite semiconductors are currently being performed to clarify this issue.

## 7.2 MOCVD growth

The utilization of metal-organic chemical vapor deposition (MOCVD) for the growth of InN layers is strongly desired for industrial application of the material thanks to its good scalability [27, 30]. Unfortunately, MOCVD grown InN still exhibits rather high electron concentrations and lower crystal quality compared to state-of-the-art MBE InN. Both, point defects such as nitrogen vacancies ($V_N$) and interstitials ($N_I$), as well as hydrogen impurities introduced in MOCVD growth through the use of $NH_3$ as the nitrogen source have been proposed as the responsible donors behind the increased electron concentrations in as-grown MOCVD InN [28, 29, 63, 128]. In MOCVD growth of InN the growth temperature is an especially delicate parameter with large impact on the material quality. It is limited on the low-temperature end by insufficient decomposition of $NH_3$, and nitrogen out-diffusion on the high-temperature end.

In order to investigate the role of the growth temperature on the incorporation of point defects in the material a set of InN layers was deposited by

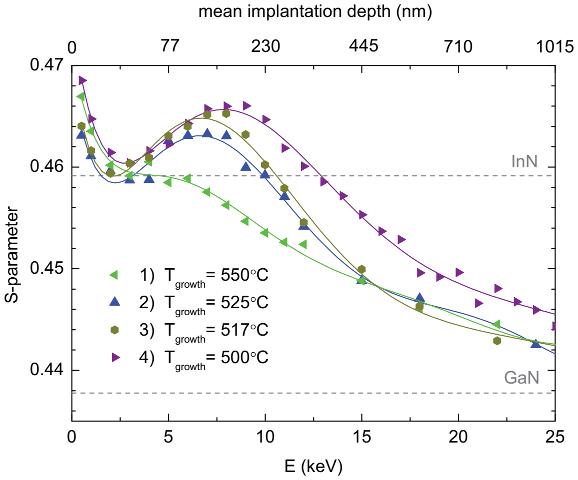

**Figure 7.2.** S-parameter of different MOCVD grown InN layers as a function of the positron implantation energy/ mean implantation depth. Characteristic values of the InN and GaN lattices are displayed for comparison. Solid lines are guides to the eye.

MOCVD on GaN templates at temperatures from 500 to 550°C. Doppler broadening measurements were performed at room temperature and the recorded line-shape S parameters are displayed in Fig. 7.2 as a function of the positron implantation energy for the investigated set of samples (Table 2.1). At low implantation energies, i.e., low mean implantation depth, most positrons annihilate at the surface of the material, which is characterized by a surface specific annihilation parameter. At around 3 keV, positrons penetrate deeper into the sample and the surface effects become negligible. The S-parameter decreases rapidly towards the value specific for the InN layer. As visible, these are in all samples close to the characteristic value for InN bulk and hence no vacancy trapping is observed. The InN reference value has been determined by measuring a reference sample in which all positrons annihilate in the delocalized state of the InN lattice. With higher implantation energies the spectrum shows for all samples except sample No.1 a strong profile with increasing S-parameter and a maximum at around 7.5 keV, i.e., a mean positron implantation depth of $\sim$ 150 nm. This indicates an increase in positron trapping to vacancy-type defects. The turning point at about half of the layer thickness [129] is caused by positrons annihilating in the GaN template and confirms well the layer thickness determined by cross-sectional SEM, i.e., 300±30 nm [27]. In sample No.1 no such profile is visible and the S-parameter approaches with higher implantation energies directly the GaN bulk value in the GaN template.

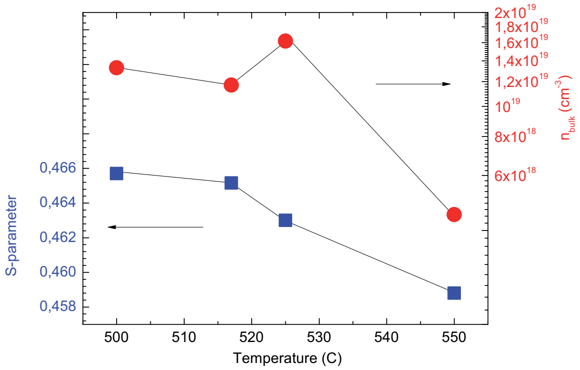

**Figure 7.3.** Effect of growth temperature on bulk electron concentration (red circles) and the near-interface S-parameter (blue squares) in MOCVD InN.

While the line-shape parameters in the near-surface region are close to the InN lattice in all samples, clear differences are visible closer to the interface. For decreasing growth temperature from 550 to 500°C, the recorded near-interface S-parameters increase from 0.459 to 0.467 (Fig. 7.3). At the same time, the estimated bulk carrier concentration increases from mid-$10^{18}$ cm$^{-3}$ to low-$10^{19}$ cm$^{-3}$ and the electron Hall mobility decreases by around one half from $\sim$1100 to 550 cm$^2$/Vs. For the sample grown at 550°C the S-parameter is close to the InN lattice and hence, no positron annihilation at vacancy defects is observed at room temperature. For samples grown at lower temperatures, the increasing S-parameter indicates the annihilation at open-volume defects. An increase in vacancy trapping is observed for decreasing growth temperature. A comparison of the recorded line-shape S and W parameter with previously identified vacancy-type positron traps in InN (Ch. 6) indicates that the dominant positron traps in the near-interface region of the investigated set of samples are $V_{\mathrm{In}}$-n$V_{\mathrm{N}}$ (n $\approx$ 2,3) clusters.

The determined near-interface S-parameters are still relatively close to the InN lattice value and the concentration of the detected vacancy complexes should not exceed low-$10^{17}$ cm$^{-3}$ in the sample grown at 500°C. The observation of $V_{\mathrm{In}}$-n$V_{\mathrm{N}}$ vacancy complexes near the interface speaks for a close proximity of $V_{\mathrm{In}}$ and $V_{\mathrm{N}}$ prior to complexing, and therefore for elevated concentrations of N vacancies in this area. Isolated nitrogen vacancies do not trap positrons in InN [112, 130] and hence escape detection with positron annihilation spectroscopy. Single $V_{\mathrm{N}}$ are singly charged donors [56] in InN. The observed increase in electron concentrations with decreasing growth temperature might therefore be explained by an increased incorporation of nitrogen vacancies, indicated by an increasing S-parameter and the deviation of the measured points from the $V_{\mathrm{In}}$-line. This is in good agreement with earlier reports on insufficient $NH_3$ decomposition at low growth temperatures [27, 29] which should promote the formation of $V_{\mathrm{N}}$ due to a lack of active nitrogen during growth. However, the applied experimental methods do not allow to rule out influences from $N_{\mathrm{I}}$ or H.

Earlier positron studies in MOCVD grown InN [70] showed an enhancement of the vacancy signal for increasing growth temperatures from 550 to 625°C, which has been attributed to beginning decomposition of the material. Assuming a direct comparability of the results, this speaks for 550°C as the optimal growth temperature in terms of suppression of $V_{\mathrm{In}}$-related defects. This is supported by Hall and photoluminescence measurements on our set of samples which show a degrading of the structural, electrical and optical properties with decreasing growth temperature [27]. Additionally, a maximum in the electron mobility is observed for this temperature [27].

# 8. Self-compensation in n-type InN

Measurements of Si-doped (Sect. 7.1.2) and irradiated InN (Sect. 7.1.1) have shown that $V_{\mathrm{In}}$-related defects are efficient positron traps in InN (Ch. 6) and are formed preferably in n-type conditions. In all investigated samples, room-temperature annihilation fractions at $V_{\mathrm{In}}$ or its complexes were found to increase with the free-electron concentration in the material, as indicated, e.g., by increasing (decreasing) line-shape S (W) parameters.

In order to be able to estimate the density of the dominant vacancy-type positron trap in a measured area of a sample, the positron trapping rate to the defect has to be known (Eq. 4.3). At moderate temperatures, positrons can get trapped additionally at Rydberg-states formed around defects with small positron binding energy (Sect. 4.1), e.g., negatively charged non-open volume defects (negative ions) or lattice sites with small effective open volume as associated to dislocations or interfaces [10]. These additional traps compete with the deep vacancy traps in positron trapping. A common way to assess positron trapping in the presence of shallow traps is the measurement of the temperature dependence of a significant annihilation parameter (line-hape, S/W parameter, positron lifetime).

Figure 8.1 shows the measured relative S-parameter in the temperature range of 150–460 K in the "layer" area (Sect. 6.3) of representative Si-doped samples with free electron concentrations from $4.5\times10^{19}$ cm$^{-3}$–$6.6\times10^{20}$ cm$^{-3}$ (Table 2.1). The observed decrease of the S-parameter at low temperatures is characteristic for competitive trapping of positrons between deep vacancy-type traps with high S-parameters, and shallow traps, with S-parameters close to the defect-free lattice. Thermal escape of positrons from loosely bound defect states and a $\mathrm{T}^{-1/2}$-dependence of the positron trapping coefficient $\mu$ for negatively charged traps [10], lead

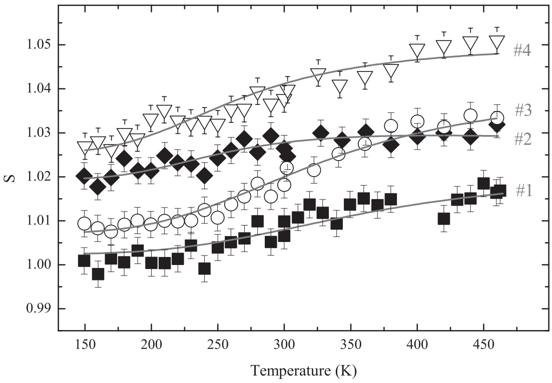

**Figure 8.1.** Temperature dependence of the S-parameters in the "layer" region ( $\bar{x}$ = 100 nm) of the Si- doped InN samples. Solid lines show fits of the spectra assuming competitive trapping between a negatively charged vacancy defect and one shallow trap.

to an overall temperature dependence of the positron annihilation spectrum which can be described with the temperature dependent positron trapping model [10]. Applying Eqs. 4.9, 4.4 and 4.5 to the case of one negatively charged vacancy and one shallow trap with characteristic relative S-parameters of $S_{\mathrm{st}}$ = $S_{\mathrm{bulk}}$ = 1 [10], the measured S-parameter is given as

$$S(T) = 1 + \frac{\kappa_{\mathrm{V}}(T)}{\frac{1}{\tau_{\mathrm{bulk}}} + \frac{\kappa_{\mathrm{st}}(T)}{1+\tau_{\mathrm{st}}\delta_{\mathrm{st}}(T)} + \kappa_{\mathrm{V}}(T)}(S_{\mathrm{V}} - 1) \tag{8.1}$$

where $\tau_{\mathrm{bulk}}$ and $\tau_{\mathrm{st}}$ are the positron lifetimes in the delocalized bulk state, and localized state at a shallow trap, respectively.

The solid lines in Fig. 8.1 show fits of the spectra using Eq. 8.1 with $m_{+}^{*}$ = 1, $\tau_{\mathrm{bulk}}$ = $\tau_{\mathrm{st}}$ = 184 ps and a characteristic relative S-parameter of $S_{\mathrm{V}}$ = 1.051 for the vacancy trap, according to Ch. 6. The shallow trap binding energy was determined as $E_{\mathrm{b}}$ = 90 meV. Resulting trapping rates range from $4.7\times10^{9}$ to $9.4\times10^{11}$ $\mathrm{s}^{-1}$ for the case of vacancies. Estimated positron trapping rates to shallow traps are $\geq 4\times10^{10}$ $\mathrm{s}^{-1}$.

In the irradiated samples, a similar temperature dependence of the lineshape parameters was observed for temperature dependent spectra from 50 to 300 K, with a characteristic decrease of the S parameter at low-temperatures. The spectra have been again fitted using the above model with one dominant vacancy and one shallow trap. Trapping rates estimated in the "layer" area of the as-irradiated films are in the range of $2.4\times10^{9}$–$2\times10^{10}$ $\mathrm{s}^{-1}$ for vacancies, and $\sim9\times10^{10}$ $\mathrm{s}^{-1}$ for shallow traps. After RTA, the trapping rates in the near-surface area drop to below $6\times10^{9}$ $\mathrm{s}^{-1}$ for vacancies and $\sim2\times10^{10}$ $\mathrm{s}^{-1}$ for shallow traps.

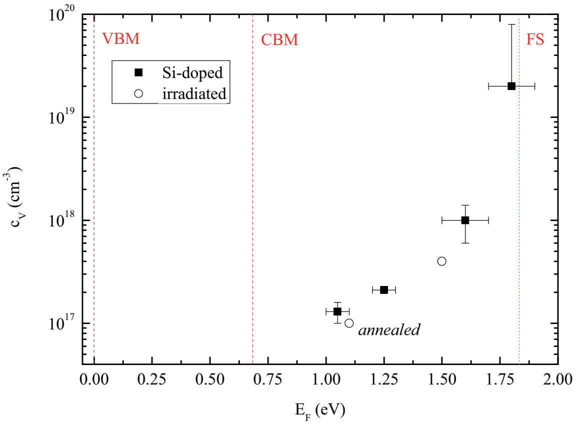

**Figure 8.2.** Estimated vacancy concentrations of Si-doped InN (full symbols) as a function of the determined bulk Fermi level. Vacancy concentrations for an irradiated sample before (higher concentration) and after annealing are given for comparison.

The concentrations of vacancies and shallow traps are directly proportional to their positron trapping rates (Eq. 4.3). Assuming a trapping coefficient of $\mu_V = \mu_{st} = 3\times10^{15}$ s$^{-1}$ at room temperature, this translates to concentrations from $5\times10^{16}$ cm$^{-3}$ to $2\times10^{19}$ cm$^{-3}$ for vacancies, and $\geq 1\times10^{18}$ cm$^{-3}$ for shallow traps. The estimated vacancy concentrations of the Si-doped samples, and an irradiated sample before and after annealing, are plotted in Fig. 8.2 as a function of the bulk Fermi-energy as determined in Ref. [37]. Although a distinction between the negative and neutral charge states is not possible in our measurements due to the strong trapping to shallow positron traps, the clear increase of the vacancy concentrations with increasing Fermi energy indicates (Sect. 3.4) that In vacancies are formed as negatively charged. Therefore, they should act as efficient compensating and scattering centers in the material.

The measured electron mobilities in the Si-doped films are shown in Fig. 8.3, together with results from irradiated InN films before and after annealing. In the Si-doped films, mobilities range from 40–1050 cm$^2$/Vs and are close to the mobilities in the irradiated films after RTA. Mobilities for as-irradiated samples are significantly lower, except for the case of very high electron concentrations. Calculated mobilities are shown in addition, and were determined using a three layer conduction model including near-surface, bulk and interface contributions [54]. For 500 nm thick films, influence from the surface is small [54, 131]. The bulk mobility ($m$) in n-type InN is dominated by ionized defect scattering, and is

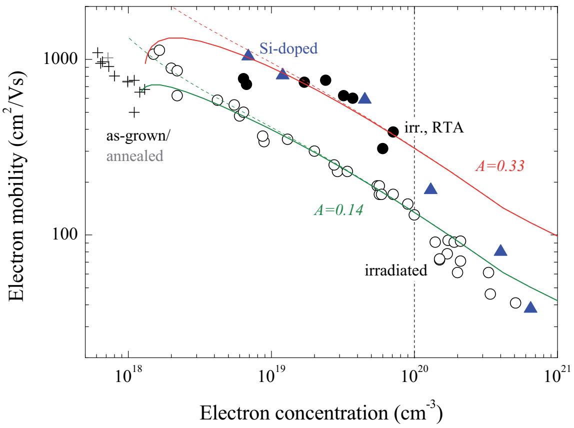

**Figure 8.3.** Measured electron mobilities of Si doped InN samples (triangles) as a function of the free electron concentration. Mobilities from as-grown (crosses) and irradiated InN samples before (open circles) and after RTA (full circles) are given for comparison (data from Refs. [60, 69]). Calculated mobilities for two different compensation schemes are shown with (solid lines) and without (dashed lines) the influence of dislocation scattering.

proportional [132] to

$$m \sim \frac{n}{Z_{\mathrm{D}}^2 N_D + Z_{\mathrm{A}}^2 N_A} = \frac{Z_{\mathrm{D}} - |Z_{\mathrm{A}}|K}{Z_{\mathrm{D}}^2 + Z_{\mathrm{A}}^2 K} =: A, \tag{8.2}$$

where $Z_{\mathrm{D}}$ and $Z_{\mathrm{A}}$ are the donor and acceptor charge, respectively, and $K = N_{\mathrm{A}}/N_{\mathrm{D}}$ is the compensation ratio. The advantage of using the proportionality constant $A$ for discussing compensation is that the defect charge and compensation ratio do not have to be fixed. At the interface, scattering due to charged dislocation lines is included, whose density was assumed to fall off exponentially with increasing distance from the interface. At moderate doping levels, the mobility data of the Si-doped samples are fitted well by calculated mobilities assuming $A = 0.33$. For comparison, as-irradiated films show much lower mobilities and are approximated best for $A = 0.14$. After RTA treatment, the mobilities in the irradiated films are close to the values for the Si-doped samples. For higher doping levels above about $n_{\mathrm{e}} = 10^{20}\mathrm{cm}^{-3}$ ($E_{\mathrm{F}}$ = 1.1 eV), the mobility in the Si-doped films starts to deviate strongly from the calculated line for $A = 0.33$ and approaches the irradiated case for the highest doped sample. In the as-irradiated material, a similar decrease in the mobility is observable but is less pronounced and a decrease to $A = 0.11$ is observed.

Using Eq. 8.2, the densities of dominant donors and acceptors in the InN films can be estimated, if their charges are known. $Si_{In}^{+}$ can be expected as dominant donors in the Si-doped samples, with possible contributions from $V_{\mathrm{N}}^{+}$ [56]. In the irradiated films, $V_{\mathrm{N}}^{+}$ [56] are assumed to be responsible for the increase in free electron concentration upon increasing irradiation doses [69]. Therefore, a donor charge of $Z_{\mathrm{D}} = 1$ can be estimated. The dominant vacancy-type acceptors in the InN samples have been probed by positron annihilation spectroscopy and were identified as $V_{\mathrm{In}}$ in the as-irradiated films, and $V_{\mathrm{In}}$-$mV_{\mathrm{N}}$ complexes ($m$≈1–3) in the Si-doped samples as well as irradiated films after RTA treatment. Additionally, a high density of shallow positron traps was found that can be formed by negatively charged defects with small or no effective open volume. DFT calculations [56] predict the $V_{\mathrm{In}}$ to be triply negatively charged. For the $V_{\mathrm{In}}$-$mV_{\mathrm{N}}$ complexes, a reduction in charge is expected [57]. The identity of the shallow traps cannot be determined in positron experiments. A comparison with DFT calculations [55, 64] suggest negatively charged $V_{\mathrm{N}}^{-}$, as well as $\mathrm{H}_{\mathrm{N}}^{-}$ as most likely candidates in highly n-type conditions. At high Fermi energies, clusters of $V_{\mathrm{N}}^{-}$ are also predicted to become energetically favorable [64].

Assuming an average charge of $Z_{\mathrm{A}} = 1$ equals compensation ratios of $K = 0.5$ for $A = 0.33$, and $K = 0.75$ for $A = 0.14$. At a free electron concentration of, e.g., $n_{\mathrm{e}} = 10^{20}$ cm$^{-3}$, this translates to donor and acceptor concentrations of $N_{\mathrm{D}} = 2 \times 10^{20}$ cm$^{-3}$ and $N_{\mathrm{A}} = 1 \times 10^{20}$ cm$^{-3}$ for $K = 0.5$, and $N_{\mathrm{D}} = 4 \times 10^{20}$ cm$^{-3}$ and $N_{\mathrm{A}} = 3 \times 10^{20}$ cm$^{-3}$ for $K = 0.75$. For higher acceptor charges, a smaller defect density leads to the same mobility behavior (e.g., $A = 0.14$, $Z_{\mathrm{A}} = 1$: $N_{\mathrm{D}} = 2.5 \times 10^{20}$ cm$^{-3}$, $N_{\mathrm{A}} = 5 \times 10^{19}$ cm$^{-3}$). The total acceptor concentrations estimated from Hall effect measurements are about 1–2 orders of magnitude higher than the values determined in temperature dependent Doppler broadening measurements. This might be explained by screening effects in the highly n-type InN samples. Screening reduces long-range Coulomb-related positron capture which could lead to severe underestimation of charged defect concentrations in positron annihilation measurements. This affects especially the estimated densities of shallow traps with no deep positron state. Also for vacancy-type defects the use of a lower positron trapping coefficient may be appropriate (e.g., $\frac{\mu_{V-}}{\mu_{V0}} \approx 3$–5, [10]), which would lead to higher estimated vacancy densities. Additionally, high dislocation densities in the material [54, 59] could lead to a constant background trapping of positrons and in turn to an underestimation of the effective trapping rates of remaining centers in Doppler broadening spectroscopy. The exceptionally low positron diffusion lengths up to high temperatures in the InN samples [59] speak in favor of such a scenario. A high compensation ratio in the Si-doped InN layers is additionally supported by the observation of strong Urbach tails in optical absorption spectra from these samples [37].

The exponential increase of the concentration of $V_{\mathrm{In}}$ and its complexes, as observed in positron annihilation measurements (Fig. 8.2), coincides with the onset of the strong deviation of the measured electron mobilities in the Si-doped samples from the calculated mobilities at a Fermi energy of $\sim$1.1 eV (Fig. 8.3). This suggests that scattering from acceptor-type defects starts to contribute strongly to the mobility behavior at elevated free electron concentrations. The observed high positron trapping rates to shallow traps indicate that $V_{\mathrm{In}}$-related defects do not account alone for the whole compensation, but additional negatively charged acceptors are present in the investigated samples in high concentrations. These might be formed by singly negatively charged $V_{\mathrm{N}}$ and multiply negatively charged $V_{\mathrm{N}}$ clusters which become increasingly favorable at high Fermi levels [64]. Indirect evidence of the presence of $V_{\mathrm{N}}$ clusters was found by the observation of $V_{\mathrm{In}}$-$mV_{\mathrm{N}}$ complexes ($m \approx 1$–3) in positron measurements of the Si-doped InN samples [112]. The lower charge of the compensating $V_{\mathrm{In}}$-$V_{\mathrm{N}}$ complexes in Si-doped samples and RTA treated irradiated layers, compared to the triply charged $V_{\mathrm{In}}$ in the as-irradiated samples, might contribute to the observed mobility drop after annealing.

The experimentally observed high acceptor densities in highly n-type InN are in sharp contrast to theoretical values based on formation energies from DFT calculations [55, 57, 64, 97]. This suggests that thermal equilibrium considerations might not be appropriate for estimating point defect concentrations in n-type InN, a material which is commonly grown at low temperatures. The formation of point defects during growth of InN is likely to be dominated by other mechanisms [59].

# 9. Summary

In this work, positron annihilation spectroscopy was used to investigate the properties of point defects in n-type InN. By combining density functional theory calculations with experimental positron annihilation methods the dominant vacancy-type positron traps in common InN material could be identified together with their characteristic positron annihilation properties.

It was found that isolated $V_{\mathrm{In}}$ and $V_{\mathrm{In}}$ complexes are efficient positron traps. $V_{\mathrm{N}}$ and pure $V_{\mathrm{N}}$ complexes, on the other hand, do not trap positrons in InN. Isolated $V_{\mathrm{In}}$ are only present in irradiated InN films and anneal out at temperatures of $\leq 475°\mathrm{C}$, if not stabilized by other point defects. Stabilization of $V_{\mathrm{In}}$ in InN was found to occur through complex formation with $V_{\mathrm{N}}$. $V_{\mathrm{In}}$-$nV_{\mathrm{N}}$ complexes were discovered the dominant vacancy-type positron trap in as-grown n-type InN samples. Towards the layer-substrate interface, enhanced formation of bigger vacancy clusters with increasing number of $V_{\mathrm{N}}$ could be observed in both as-grown and irradiated material after annealing which indicates that the InN/GaN interface acts as a sink for vacancy defects. High concentrations of additional $V_{\mathrm{N}}$ and $V_{\mathrm{N}}$ complexes are expected in that area. Additionally, a correlation with elevated dislocation densities at the interface was found. Density functional theory calculations of strained InN supercells simulating the effect screw-type dislocations could find no significant effect of the strain on the formation energy of vacancy defects, however.

In low-temperature MOCVD growth of InN a degrading of the structural, electrical and optical properties with decreasing growth temperatures from 550 to 500°C could be observed. This was accompanied by an increase in the formation of mixed $V_{\mathrm{In}}$ $V_{\mathrm{N}}$ complexes near the interface. A comparison with earlier positron measurements speaks for 550°C as the optimal growth temperature in terms of vacancy suppression in MOCVD InN.

The densities of dominant vacancy and negative-ion type acceptors in Si-doped and irradiated n-type InN were estimated by temperature-dependent Doppler broadening measurements and compared to Hall mobility of samples with increasing free carrier concentrations up to $n_{\mathrm{e}}$ = $6.6\times10^{20}$ $\mathrm{cm}^{-3}$. Significant compensation of n-type InN is found for high Fermi level positions, which is attributed to the presence of negatively charged indium vacancy complexes and additional acceptor-type defects with small or no effective open volume that might be formed by negatively charged nitrogen vacancies and their complexes. Estimated densities of native point defects in InN are far away from what can be expected from thermodynamic considerations. This suggests that alternative defect formation mechanisms determine point defect concentrations in the material.

# Bibliography

[1] http://newsroom.intel.com/docs/DOC 1047. Intel Xeon 7500, Presskit.

[2] A. Hangleiter. *Mrs Bulletin*, 28:350, 2003.

[3] B. Monemar. *J. Mater. Sci. Mater. Electron.*, 10:227, 1999.

[4] J. Wu. *J. Appl. Phys.*, 106:011101, 2009.

[5] A. G. Bhuiyan, A. Hashimoto, and A. Yamamoto. *J. Appl. Phys.*, 94:2779, 2003.

[6] T. L. Tansley and C. P. Foley. *J. Appl. Phys*, 59:3241, 1986.

[7] V. Yu. Davydov, A. A. Klochikhin, R. P. Seisyan, V. V. Emtsev, S. V. Ivanov, F. Bechstedt, J. Furthmüller, H. Harima, A. V. Mudryi, J. Aderhold, O. Semchinova, and J. Graul. *Phys. Status Solidi B*, 229:R1, 2002.

[8] V. Y. Davydov, A. A. Klochikhin, V. V. Emtsev, S. V. Ivanov, V. V. Vekshin, F. Bechstedt, J. Furthmüller, H. Harima, A. V. Mudryi, A. Hashimoto, A. Yamamoto, J. Aderhold, J. Graul, and E. E. Haller. *Phys. Status Solidi B*, 230:R4, 2002.

[9] R. Krause-Rehberg and H. S. Leipner. *Positron Annihilation in Semiconductors*. Springer, 1998.

[10] M. J. Puska, C. Corbel, and R. M. Nieminen. *Phys. Rev. B*, 41:9980, 1990.

[11] M. J. Puska and R. M. Nieminen. *Rev. Mod. Phys.*, 66:841, 1994.

[12] K. Saarinen, P. Hautojärvi, and C. Corbel. *Positron Annihilation Spectroscopy of Defects in Semiconductors*, volume 51A of *Semiconductors and Semimetals*. Academic Press, New York, 1998.

[13] E. F. Schubert. *Light Emitting Diodes*. Cambridge University Press, Cambridge, 2nd edition, 2006.

[14] J. Wu, W. Walukiewicz, W. Shan, K. M. Yu, J. W. Ager III, S. X. Li, E. E. Haller, Hai Lu, and William J. Schaff. *J. Appl. Phys.*, 94:4457, 2003.

[15] S. F. Chichibu, A. Uedono, T. Onuma, B. A. Haskell, A. Chakraborty, T. Koyama, P. T. Fini, S. Keller, S. P. DenBaars, J. S. Speck, U. K. Mishra, S. Nakamura, S. Yamaguchi, S. Kamiyama, H. Amano, I. Akasaki, J. Han, and T. Sota. *Nature Mat.*, 5:810, 2006.

[16] S. Strite and H. Morkoc. *Journal of Vacuum Science Technology B: Microelectronics and Nanometer Structures*, 10:1237, 1992.

[17] J. H. Edgar, editor. *Properties of Group-III Nitrides*, volume EMIS Datareviews Series. IEE, London, 1994.

[18] O. Ambacher. *J. Phys. D*, 31:2653, 1998.

[19] I. Mahboob, T. D. Veal, C. F. McConville, H. Lu, and W. J. Schaff. *Phys. Rev. Lett.*, 92:036804, 2004.

[20] H. Lu, W. J. Schaff, L. F. Eastman, and C. E. Stutz. *Appl. Phys. Lett.*, 82:1736, 2003.

[21] M. T. Hasan, A. G. Bhuiyan, and A. Yamamoto. *Solid-State Electronics*, 52:134, 2008.

[22] V. M. Polyakov and F. Schwierz. *J. Appl. Phys*, 101:033703, 2007.

[23] N. Teraguchi and A. Suzuki. Nitride-type III-V HEMT having an InN 2DEG channel layer, 2001. US Patent 6,177,685.

[24] Y. Nanishi, S. Yoshiki, and T. Yamaguchi. *Jpn. J. Appl. Phys.*, 42:2549, 2003.

[25] H. Lu, W. J. Schaff, J. Hwang, H. Wu, W. Yeo, A. Pharkya, and L. F. Eastman. *Appl. Phys. Lett.*, 77:2548–2550, 2000.

[26] C. S. Gallinat, G. Koblmüller, J. S. Brown, and J. S. Speck. *J. Appl. Phys.*, 102:064907, 2007.

[27] Ö. Tuna, H. Behmenburg, C. Giessen, R. H. Kalisch, G. P. Yablonski, and M. Heuken. *Phys. Status Solidi C*, 8:2044, 2011.

[28] S. Ruffenach, M. Moret, O. Briot, and B. Gil. *Appl. Phys. Lett.*, 95:042102, 2009.

[29] A. Yamamoto, K. Sugita, and A. Hashimoto. *J. Cryst. Growth*, 311:4636, 2009.

[30] S. Ruffenach, M. Moret, O. Briot, and B. Gil. *Phys. Status Solidi A*, 207:9, 2010.

[31] H. J. Scheel, T. Fukuda, and J. Wiley. *Crystal growth technology*. Wiley Online Library, 2003.

[32] C. J. Lu, L. A. Bendersky, H. Lu, and W. J. Schaff. *Appl. Phys. Lett.*, 83:2817, 2003.

[33] C. S. Gallinat, G. Koblmüller, and J. S. Speck. *Appl. Phys. Lett.*, 95:022103, 2009.

[34] H. Lu, W. J. Schaff, J. Hwang, H. Wu, G. Koley, and L. F. Eastman. *Appl. Phys. Lett.*, 79:1489–1491, 2001.

[35] E. Sakalauskas, P. Schley, J. Räthel, T. A. Klar, R. Müller, J. Pezoldt, K. Tonisch, J. Grandal, M. A. Sanchez-Garcia, E. Calleja, A. Vilalta-Clemente, P. Ruterana, and R. Goldhahn. *Phys. Status Solidi A*, 207:1066, 2010.

[36] S. Wei, X. Nie, I. G. Batyrev, and S. B. Zhang. *Phys. Rev. B*, 67:165209, 2003.

[37] P. D. C. King, T. D. Veal, P. H. Jefferson, S. A. Hatfield, L. F. J. Piper, C. F. McConville, F. Fuchs, J. Furthmüller, F. Bechstedt, H. Lu, and W. J. Schaff. *Phys. Rev. B*, 77:045316, 2008.

[38] F. Bernardini, V. Fiorentini, and D. Vanderbilt. *Phys. Rev. B*, page R10024, 1997.

[39] J. Furthmüller, P. H. Hahn, F. Fuchs, and F. Bechstedt. *Phys. Rev. B*, 72:205106, 2005.

[40] C. Hsiao, T. Liu, C. Wu, H. Hsu, G. Hsu, L. Chen, W. Shiao, C. Yang, A. Gaellstroem, P. Holtz, C. Chen, and K. Chen. *Appl. Phys. Lett.*, 92:111914, 2008.

[41] K. Nishida, Y. Kitamura, Y. Hijikata, H. Yaguchi, and S. Yoshida. *Phys. Status Solidi B*, 241:2839, 2004.

[42] V. Cimalla, J. Pezoldt, G. Ecke, R. Kosiba, O. Ambacher, L. Spiess, G. Teichert, H. Lu, and W. J. Schaff. *Appl. Phys. Lett.*, 83:3468–3470, 2003.

[43] P. Y. Yu and M. Cardona. *Fundamentals of Semiconductors: Physics and Materials Properties*. Springer-Verlag, Berlin, 1999.

[44] E. O. Kane. *J. Phys. Chem.*, 1:249, 1957.

[45] J. Wu, W. Walukiewicz, W. Shan, K. M. Yu, J. W. Ager, E. E. Haller, Hai Lu, and W. J. Schaff. *Phys. Rev. B*, 66:201403, 2002.

[46] S. H. Wei and A. Zunger. *Appl. Phys. Lett.*, 72:2011, 1998.

[47] S. X. Li, K. M. Yu, J. Wu, R. E. Jones, W. Walukiewicz, J. W. Ager, W. Shan, E. E. Haller, Hai Lu, and William J. Schaff. *Phys. Rev. B*, 71:161201, 2005.

[48] A. Schleife, F. Fuchs, C. Rödl, J. Furthmüller, and F. Bechstedt. *Appl. Phys. Lett.*, 94:012104, 2009.

[49] W. Walukiewicz. *Physica B*, 302-303:123–134, 2001.

[50] W. Walukiewicz. *Appl. Phys. Lett.*, 54:2094–2096, 1989.

[51] P. A. Anderson, C. H. Swartz, D. Carder, R. J. Reeves, S. M. Durbin, S. Chandril, and T. H. Myers. *Appl. Phys. Lett.*, 89:184104, 2006.

[52] J. Wu, W. Walukiewicz, S. X. Li, R. Armitage, J. C. Ho, E. R. Weber, E. E. Haller, Hai Lu, William J. Schaff, A. Barcz, and R. Jakiela. *Appl. Phys. Lett.*, 84:2805–2807, 2004.

[53] T. S. Moss. *Proceedings of the Physical Society. Section B*, 67:775, 1954.

[54] P. D. C. King, T. D. Veal, and C. F. McConville. *J. Phys. Cond. Matt.*, 21:174201, 2009.

[55] C. G. Van de Walle, J. L. Lyons, and A. Janotti. *Phys. Status Solidi A*, 207:1024, 2010.

[56] C. Stampfl, C. G. Van de Walle, D. Vogel, P. Krüger, and J. Pollmann. *Phys. Rev. B*, 61:R7846–R7849, 2000.

[57] X. M. Duan and C. Stampfl. *Phys. Rev. B*, 79:174202, 2009.

[58] A. Janotti and C. G. Van de Walle. 92:032104, 2008.

[59] C. Rauch, F. Tuomisto, A. Vilalta-Clemente, B. Lacroix, P. Ruterana, S. Kraeusel, and W. Schaff. *Appl. Phys. Lett.*, 100:091907, 2012.

[60] R. E. Jones, S. X. Li, L. Hsu, K. M. Yu, W. Walukiewicz, Z. Liliental-Weber, J. W. Ager III, E. E. Haller, H. Lu, and W. J. Schaff. *Physica B*, 376:436, 2006.

[61] L. F. J. Piper, T. D. Veal, C. F. McConville, H. Lu, and W. J. Schaff. *Appl. Phys. Lett.*, 88:252109, 2006.

[62] H. Wang, D. S. Jiang, L. L. Wang, X. Sun, W. B. Liu, D. G. Zhao, J. J. Zhu, Z. S. Liu, Y. T. Wang, S. M. Zhang, and H. Yang. *J. Phys. D*, 41:135403, 2008.

[63] K. S. A. Butcher, A. J. Fernandes, P. P.-T. Chen, M. Wintrebert-Fouquet, H. Timmers, S. K. Shrestha, H. Hirshy, R. M. Perks, and Brian F. Usher. *J. Appl. Phys.*, 101:123702, 2007.

[64] X. M. Duan and C. Stampfl. *Phys. Rev. B*, 77:115207, 2008.

[65] F. Tuomisto, A. Pelli, K. M. Yu, W. Walukiewicz, and W. J. Schaff. *Phys. Rev. B*, 75:193201, 2007.

[66] W. Walukiewicz, R.E. Jones, S.X. Li, K.M. Yu, J.W. Ager III, E.E. Haller, H. Lu, and W.J. Schaff. *J. Cryst. Growth*, 288:278 – 282, 2006. Proceedings of the Second ONR International Indium Nitride Workshop Kailua-Kona, Hawaii 9-13 January 2005.

[67] R. E. Jones, K. M. Yu, S. X. Li, W. Walukiewicz, J. W. Ager, E. E. Haller, H. Lu, and W. J. Schaff. *Physical Review Letters*, 96:125505, 2006.

[68] W. J. Schaff, H. Lu, L. F. Eastman, W. Walukiewicz, K. M. Yu, S. Keller, S. Kurtz, B. Keyes, and L. Gevilas. In H. M. Ng and A. G. Baca, editors, *State-of-the-Art Program on Compound Semiconductors XLI and Nitride and Wide Bandgap Semiconductors for Sensors, Photonics, and Electronics V*, volume 2004-06 of *The Electrochemical Society Proceedings Series*, page 358, Honolulu, HI, 2004. Electrochemical Society.

[69] R. E. Jones, S. X. Li, E. E. Haller, H. C. M. van Genuchten, K. M. Yu, J. W. Ager III, Z. Liliental-Weber, W. Walukiewicz, H. Lu, and W. J. Schaff. *Appl. Phys. Lett.*, 90:162103, 2007.

[70] A. Pelli, K. Saarinen, F. Tuomisto, S. Ruffenach, and O. Briot. *Appl. Phys. Lett.*, 89:011911, 2006.

[71] B. Maleyre, O. Briot, and S. Ruffenach. *J. Cryst. Growth*, 269:15, 2004.

[72] www.aixtron.com.

[73] H. Föll. Defects in Crystals. Hyperscript (www.tf.uni-kiel.de).

[74] M. Lannoo and J. Bourgoin. *Point defects in Semiconductors I*. Springer, Berlin, 1981.

[75] F. Agullo-Lopez, C. R.A. Catlow, and P. D. Townsend. *Point defects in materials*. Academic press, London, 1988.

[76] S. T. Pantelides. *Rev. Mod. Phys.*, 50:797, 1978.

[77] S. T. Pantelides, editor. *Deep centers in semiconductors*. Gordon and Breach Science Publishers, 1986.

[78] C. A. J. Ammerlaan, W. Bergholz, and M. Schulz. *Impurities and defects in group IV elements and III-V compounds*. Number 22 in Landolt-Börnstein: Numerical Data and Functional Relationships in Science and Technology Series. Springer-Verlag, Berlin, 1989.

[79] C . G. Van de Walle and J. Neugebauer. *J. Appl. Phys.*, 95:3851–3879, 2004.

[80] C. G. Van de Walle and J. Neugebauer. *J. Appl. Phys.*, 95:3851–3879, 2004.

[81] J. Tersoff. *Phys. Rev. B*, 30:4874, 1984.

[82] W. Mönch. *Electronic properties of semiconductor interfaces*. Springer-Verlag, Berlin, 2004.

[83] J. Tersoff. *Phys. Rev. Lett.*, 58:2367, 1987.

[84] C. G. Van de Walle and J. Neugebauer. *Nature*, 423:626, 2003.

[85] M. Lannoo and J. Bourgoin. *Point defects in Semiconductors II*. Springer, Berlin, 1983.

[86] M. Stavola, editor. *Identification of defects in semiconductors*, volume 51B of *Semiconductors and Semimetals*. Academic Press, New York, 1999.

[87] P. A. M Dirac. *Proc. R. Soc. Lond. A*, 11:610–624, 1928.

[88] C. D. Anderson. *Phys. Rev.*, 43:491, 1933.

[89] K. G. Lynn, J. R. MacDonald, R. A. Boie, L. C. Feldman, J. D. Gabbe, M. F. Robbins, E. Bonderup, and J. Golovchenko. *Phys. Rev. Lett.*, 38:241–244, 1977.

[90] M. Alatalo, B. Barbiellini, M. Hakala, H. Kauppinen, T. Korhonen, M. J. Puska, K. Saarinen, P. Hautojärvi, and R. M. Nieminen. *Phys. Rev. B*, 54:2397, 1996.

[91] K. Saarinen. *Characterization of native point diefects in GaN by positron annihilation spectroscopy*. Elsevier, Amsterdam, 2000.

[92] F. Reurings. *Slow positrons in material science: pulsed positron beam and defect studies in Indium Nitride*. PhD thesis, Aalto University, 2010.

[93] A. F. Makhov. *Sov. Phys.-Solid State*, 2:1934, 1960.

[94] A. Vehanen, K. Saarinen, P. Hautojärvi, and H. Huomo. *Phys. Rev. B*, 35:4606, 1987.

[95] A. van Veen, H. Schut, M. Clement, J. M. M. de Nijs, A. Kruseman, and M. R. IJpma. *Appl. Surf. Sci.*, 85:216, 1995.

[96] R. M. Martin. *Electronic structure: basic theory and practical methods*. Cambridge University Press, 2004.

[97] X. M. Duan and C. Stampfl. *Phys. Rev. B*, 79:035207, 2009.

[98] M. J. Puska and R. M. Nieminen. *J. Phys. F*, 13:333, 1983.

[99] H. E. Hansen, R. M. Nieminen, and M. J. Puska. *J. Phys. F*, 14:1299–1316, 1984.

[100] E. Boroński and R. M. Nieminen. *Phys. Rev. B*, 34:3820, 1986.

[101] I. Makkonen, M. Hakala, and M. J. Puska. *Phys. Rev. B*, 73:035103, 2006.

[102] P. Hohenberg and W. Kohn. *Physical Review*, 136:B864, 1964.

[103] W. Kohn, L.J. Sham, et al. *Phys. Rev*, 140:A1133–A1138, 1965.

[104] A. Laakso, J. Oila, A. Kemppinen, K. Saarinen, W. Egger, L. Liszkay, P. Sperr, H. Lu, and W. J. Schaff. *J. Cryst. Growth*, 269:41–49, 2004.

[105] J. Oila, A. Kemppinen, A. Laakso, K. Saarinen, W. Egger, L. Liszkay, P. Sperr, H. Lu, and W. J. Schaff. *Appl. Phys. Lett.*, 84:1486, 2004.

[106] A. Uedono, S. F. Chichibu, M. Higashiwaki, T. Matsui, T. Ohdaira, and R. Suzuki. *J. Appl. Phys.*, 97:043514, 2005.

[107] C. Rauch, F. Reurings, F. Tuomisto, T. D. Veal, C. F. McConville, H. Lu, W. J. Schaff, C. S. Gallinat, G. Koblmüller, J. S. Speck, W. Egger, B. Löwe, L. Ravelli, and S. Sojak. *Phys. Status Solidi A*, 207:1083, 2010.

[108] S. Hautakangas, V. Ranki, I. Makkonen, M. J. Puska, K. Saarinen, L. Liszkay, D. Seghier, H. P. Gislason, J. A. Freitas, R. L. Henry, X. Xu, and D. C. Look. *Physica B-Condensed Matter*, 376:424, 2006.

[109] P. E. Blöchl. *Phys. Rev. B*, 50:17953–17979, 1994.

[110] G. Kresse and J. Furthmüller. *Phys. Rev. B.*, 54:11169, 1996.

[111] F. Reurings, C. Rauch, F. Tuomisto, R. E. Jones, K. M. Yu, W. Walukiewicz, and W. J. Schaff. *Phys. Rev. B*, 82:153202, 2010.

[112] C. Rauch, I. Makkonen, and F. Tuomisto. *Phys. Rev. B*, 84:125201, 2011.

[113] F. Reurings, F. Tuomisto, W. Egger, B. Loewe, L. Ravelli, S. Sojak, Z. Liliental-Weber, R. E. Jones, K. M. Yu, W. Walukiewicz, and W. J. Schaff. *Phys. Status Solidi A*, 207:1087, 2010.

[114] S. Hautakangas, I. Makkonen, V. Ranki, J. Puska, K. Saarinen, X. Xu, and D. C. Look. *Phys. Rev. B*, 73:193301, 2006.

[115] F. Reurings, F. Tuomisto, C. S. Gallinat, G. Koblmüller, and J. S. Speck. *Appl. Phys. Lett.*, 97:251907, 2010.

[116] K. Saarinen, T. Laine, S. Kuisma, J. Nissila, P. Hautojarvi, L. Dobrzynski, J. M. Baranowski, K. Pakula, R. Stepniewski, M. Wojdak, A. Wysmolek, T. Suski, M. Leszczynski, I. Grzegory, and S. Porowski. *Physical Review Letters*, 79:3030, 1997.

[117] Z. Liliental-Weber, R.E. Jones, H.C.M. van Genuchten, K.M. Yu, W. Walukiewicz, J.W. Ager III, E.E. Haller, H. Lu, and W.J. Schaff. *Physica B*, 401:646, 2007.

[118] S. Limpijumnong and C. G. Van de Walle. *Phys. Rev. B*, 69:035207, 2004.

[119] F. Tuomisto, T. Paskova, R. Kroger, S. Figge, D. Hommel, B. Monemar, and R. Kersting. *Appl. Phys. Lett.*, 90:121915, 2007.

[120] J.-M. Mäki, I. Makkonen, F. Tuomisto, A. Karjalainen, S. Suihkonen, J. Räisänen, T. Yu. Chemekova, and Yu. N. Makarov. *Phys. Rev. B*, 84:081204, 2011.

[121] A. Uedono, H. Nakamori, K. Narita, J. Suzuki, X. Wang, S. B. Che, Y. Ishitani, A. Yoshikawa, and S. Ishibashi. *J. Appl. Phys.*, 105:054507, 2009.

[122] Y. Arroyo Rojas Dasilva, M. P. Chauvat, P. Ruterana, L. Lahourcade, E. Monroy, and G. Nataf. *J. Phys. Cond. Matt.*, 22:355802, 2010.

[123] S. Kraeusel, C. Rauch, and B. Hourahine. unpublished.

[124] J. Oila, J. Kivioja, V. Ranki, K. Saarinen, D. C. Look, R. J. Molnar, S. S. Park, S. K. Lee, and J. Y. Han. *Appl. Phys. Lett.*, 82:3433, 2003.

[125] S. Kraeusel and B. Hourahine. unpublished.

[126] E. Tengborn, M. Rummukainen, F. Tuomisto, K. Saarinen, M. Rudzinski, P. R. Hageman, P. K. Larsen, and A. Nordlund. *Appl. Phys. Lett.*, 89:091905, 2006.

[127] C. Rauch, F. Tuomisto, P. D. C. King, T. D. Veal, H. Lu, and W. Schaff. unpublished.

[128] V. Darakchieva, M.-Y. Xie, D. Rogalla, H.-W. Becker, K. Lorenz, E. Alves, S. Ruffenach, M. Moret, and O. Briot. *Phys. Status Solidi A*, 208:1179, 2011.

[129] A. Zubiaga, J. A. Garcia, F. Plazaola, F. Tuomisto, J. Zuniga-Perez, and V. Munoz-Sanjose. *Phys. Rev. B*, 75:205305, 2007.

[130] C. Rauch, I. Makkonen, and F. Tuomisto. *Phys. Status Solidi A*, 208:1548, 2011.

[131] D. C. Look, H. Lu, W. J. Schaff, J. Jasinski, and Z. Liliental-Weber. *Appl. Phys. Lett.*, 80:258–260, 2002.

[132] D. C. Look, K. D. Leedy, L. Vines, B. G. Svensson, A. Zubiaga, F. Tuomisto, D. R. Doutt, and L. J. Brillson. *Phys. Rev. B*, 84:115202, 2011.

# Errata

## Publication III

On page 4, it is stated that $V_N$ are in the 3+ charge state for most of the Fermi-level positions. However, a triply positive charge is only expected for highly p-type conditions [55, 56], and $V_N$ are supposed to be in the 1+ charge state otherwise. At very high electron concentrations, a 1- charge state is predicted.

## Publication IV

On page 3, it is written that single $V_N$ are triply charged donors. This is misleading, because the lowest energy charge state for most of the Fermi level positions is 1+. Therefore, $V_N$ should commonly appear as singly charged donors.

Aalto-DD 52/2012

ISBN 978-952-60-4606-8
ISBN 978-952-60-4607-5 (pdf)
ISSN-L 1799-4934
ISSN 1799-4934
ISSN 1799-4942 (pdf)

**Aalto University**
**School of Science**
**Department of Applied Physics**
**www.aalto.fi**

BUSINESS +
ECONOMY

ART +
DESIGN +
ARCHITECTURE

SCIENCE +
TECHNOLOGY

CROSSOVER

**DOCTORAL**
**DISSERTATIONS**